Strength of the H2O near-infrared absorption bands in hydrated minerals: Effects of measurement geometry

Antoine Pommerol, Bernard Schmitt

Strength of the H_2O near-infrared absorption bands in hydrated minerals: Effects of measurement geometry

Antoine Pommerol[1] and Bernard Schmitt[1]

Received 19 May 2008; revised 16 September 2008; accepted 30 September 2008; published 17 December 2008.

[1] Quantitative effects of incidence and emergence angles variations on the 1.9- and 3-μm H_2O bands are experimentally investigated for two hydrated minerals: smectite and altered volcanic tuff. Near-infrared bidirectional reflectance spectra are measured with various incidence and emergence angles leading to phase angles varying between 10° and 140°. We observe a decrease of both band strengths when phase angle increases. The relationship between band strength and phase angle depends on both the absorption intensity, i.e., strong or weak band, and the particle size of the material. We compare experimental results with radiative transfer modeling with optical constants of a smectite. Numerical models can reproduce the changes in band strength with incidence and emergence angles if the value of the single particle scattering anisotropy varies over the absorption band. We attribute this wavelength-dependent scattering effect to enhanced surface scattering within the absorption bands compared to volume scattering outside the bands. Relative variations of band strength induced by measurement geometry variations can reach tens of percent at high phase angle. Therefore these effects have to be taken into account when mapping spectral parameters on a planetary surface or comparing spectral parameters between two surfaces if measurement geometries are subject to large variations.

Citation: Pommerol, A., and B. Schmitt (2008), Strength of the H_2O near-infrared absorption bands in hydrated minerals: Effects of measurement geometry, *J. Geophys. Res.*, *113*, E12008, doi:10.1029/2008JE003197.

1. Introduction

[2] Reflectance spectroscopy in the visible and near infrared spectral ranges (0.4–5 μm) is widely used in the field of planetary remote sensing to assess physical, mineralogical and chemical properties of various types of Solar System bodies surfaces. In most cases, the measured reflectance spectra are bidirectional because light is incident from a particular direction (position of the sun) and the light reflected by the surface is also measured along a particular direction (position of the detector). Contrasting with the hypothetical case of a Lambertian surface, all natural particular surfaces show a more or less pronounced directional anisotropy of the reflected light intensity. Therefore measured reflectance spectra are dependent on the position of both the light source and the detector.

[3] Reflectance spectra of the surfaces of various Solar System objects have been measured under different incidence and emergence angles both from the Earth-based telescopes and from cameras and spectrometers on board space probes. In order to interpret these data sets in terms of surface physical properties, different bidirectional radiative transfer models have been developed [*Hapke*, 1993; *Douté and Schmitt*, 1998; *Grundy et al.*, 2000; *Hapke*, 2002; *Shkuratov and Grynko*, 2005]. Their validity can be tested using laboratory experiments [e.g., *Douté et al.*, 2003; *Cord et al.*, 2003, 2005; *Shepard and Helfenstein*, 2007]. Experimental results allow the determination of the range of validity of the numerical models and give invaluable indications of the way they could be improved. Many experimental studies have been conducted to examine the scattering phase functions of a variety of samples in the laboratory. The influence on the scattering phase function of many parameters such as different scales of roughness, particle size, mineralogical composition, moisture content were examined [*Mustard and Pieters*, 1989; *Kamei and Nakamura*, 2002; *Cord et al.*, 2003, 2005; *Shkuratov et al.*, 2005; *Johnson et al.*, 2007; *Gunderson et al.*, 2007]. However, these experimental studies were often conducted either at one unique wavelength or in a few wavelength bands over a restricted wavelength range (visible or near infrared up to 2.5 μm). Only a few data sets of experimental spectra have been measured over large wavelength ranges, with spectral sampling comparable with on-board spectro meters and under various measurement geometries [*Pieters*, 1983; *Gradie and Veverka*, 1986; *Mustard and Pieters*, 1989; *Georgiev and Butler*, 2005; *Cloutis et al.*, 2007]. These studies highlight the wavelength dependence of the scattering phase function and/or the influence of the illumination-observation geometry on the strength of the absorption bands, that is one of the key parameters used to determine the composition of planetary surfaces. The need for laboratory measurements of bidirectional reflectance spectra under the largest variety of incidence, emergence and azimuth angles and for wavelength range and spectral

[1]Laboratoire de Planétologie de Grenoble, Université J. Fourier, CNRS/INSU, Grenoble, France.

0148-0227/08/2008JE003197

sampling comparable with instruments on-board various space probes was one of the motivation for the development of an original instrument dedicated to this purpose at Laboratoire de Planétologie de Grenoble. The LPG spectro-gonio-radiometer [*Brissaud et al.*, 2004] is designed to measure bidirectional reflectance spectra of samples over most of the solar reflected light wavelength range (0.3–4.8 μm) with high photometric accuracy at almost any possible incidence, emergence and azimuth angles.

[4] In this study, we present laboratory measurements of hydrated minerals near-infrared reflectance spectra. Water linked to minerals (adsorbed water, structural water, fluid inclusions...) is responsible for strong absorptions in this wavelength range [e.g., *Ryskin*, 1974]. These absorption bands are used to identify and characterize mineral hydration of a variety of terrestrial materials as well as on Mars' surface [e.g., *Bibring et al.*, 2006; *Jouglet et al.*, 2007; *Milliken et al.*, 2007], asteroids [e.g., *Rivkin et al.*, 2003] and outer solar system moons [e.g., *Calvin and Clark*, 1993; *McCord et al.*, 1999]. Imaging spectrometers such as OMEGA (Mars Express) and CRISM (MRO) allow local and global mapping of the strength of these absorption bands on the Martian surface that are interpreted in terms of Martian geological history. The increasing number of asteroid observations in the near infrared enables a comparison of hydration band strength between different asteroids and classes of asteroid on a large data set. Differences in band strength values can then be discussed in terms of aqueous alteration of the initial material. However, because reflectance spectra are often measured under different geometries in the case of non-resolved observations, or under continuously changing geometries from a pixel to another in the case of observations by imaging spectrometers, it is crucial to understand how band strength is related to measurement geometry.

[5] In the laboratory, we measured the bidirectional reflectance spectra of two kinds of hydrated minerals: a smectite (Montmorillonite STx-1 from Source Clay Society) and an altered volcanic tuff (Corent, volcanic province of Puy de Dôme, France) at various incidence and emergence angles resulting in phase angles varying between 10° and 140°. In addition to these laboratory measurements, we used radiative transfer modeling to examine the effects of measurement geometry on the H_2O near-infrared band strengths. We run the LPG radiative transfer model [*Douté and Schmitt*, 1998], using the optical constants of a smectite [*Roush*, 2005] to obtain bidirectional reflectance spectra in the same geometrical configurations than measured spectra. The same spectral criteria used to estimate the strength of H_2O bands are calculated on both experimental and numerical data sets, and compared.

2. Methods

2.1. Experimental Approach

2.1.1. Samples Nature and Preparation

2.1.1.1. Samples

[6] The majority of the laboratory measurements presented in this paper were performed on two different types of minerals: smectite STx-1 and volcanic tuff.

[7] The STx-1 smectite is a montmorillonite. Chemical composition as well as mineralogical information and physical properties are detailed in the study of *Costanzo and Guggenheim* [2001] and companion articles. The sample received from Source Clay Repository is an extremely fine powder. We tried to extract different particles size fractions from this powder but the totality of the powder passes through our finest sieve (25 μm). The clay mineral society indicates that purchased samples are sieved through a 2-μm sieve. However, the extremely fine smectite particles spontaneously form unconsolidated agglomerates. Therefore it is extremely difficult to give an estimate of the actual size of agglomerates that is pertinent for light scattering. We measured a relative mass loss of 14.6 % after heating the smectite at 300°C overnight (no further change in mass was measured for longer times). This loss is attributed to water (surface adsorption and interlayer water). Measurements presented by *Guggenheim and Van Groos* [2001] on another STx-1 sample show similar values.

[8] Altered volcanic tuff was collected in the young volcanic province of Corent, Puy-de-Dôme, France. This material is a good spectral analogue for the Martian surface as it is highly oxidized and does not exhibit major spectral features in the near infrared except the strong 3-μm hydration absorption. The only visible crystals are millimeter-size pyroxenes (augite). Information from the geological map (geological map of France at 1/50.000 scale, edited by the French BRGM, ''Bureau de Recherches Géologiques et Minières'') indicates that this material was formed recently (3 My) during an explosive eruption caused by the interaction between magma and water. Near-infrared spectra reveal weak absorptions around 2.2 μm and at 2.75 μm attributed to hydroxyl ions probably present in poorly crystallized phyllosilicate phases. The volcanic tuff was ground by hand using a mortar and pestle and then dry sieved to separate 9 fractions with different grain sizes, from less than 25 μm to more than 800 μm.

[9] We also measured a limited set of spectra of the SWy-2 Montmorillonite from Source Clay Repository [see *Costanzo and Guggenheim*, 2001 for details]. This sample consisted of a heterogeneous powder that was dry sieved to extract different particle size fractions (agglomerates of smaller particle).

[10] All samples used in this paper were also used in a companion paper [*Pommerol and Schmitt*, 2008] dedicated to the effect of particle size and albedo on the absorption bands. Detailed descriptions of the samples and pictures under binocular microscope are also provided in this paper.

2.1.1.2. Surface Preparation

[11] Measurement of bidirectional reflectance spectra at emission angles up to 70° requires a sample surface that is at least 6 cm long and 2 cm wide on the LPG spectro-gonio-radiometer. The sample holders were always larger than these values and filled with sample material with a physical thickness large enough so that the optical depth at all measured wavelengths can be considered as infinite. This is easily verified by comparing spectra of the same sample but with increasing depths. Optical depth is considered as infinite when no more change between successive spectra is observed. This generally requires less than 1 mm to occur. In practice, measured samples were always at least a few millimeters thick.

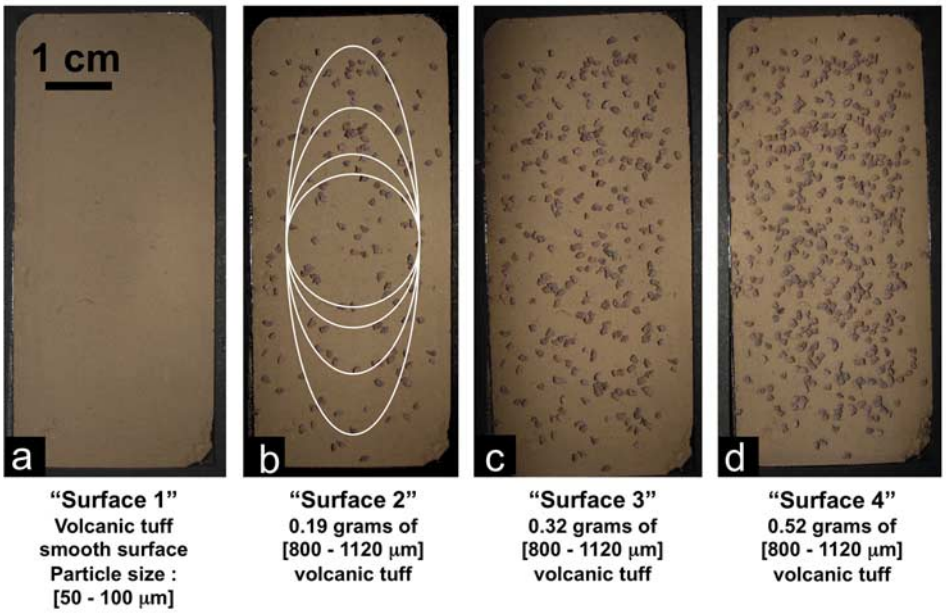

Figure 1. Synthetic image consisting in four photographic images of different surfaces prepared with two particle size fractions of the volcanic tuff sample: [50–100 μm] and [800–1120 μm]. (a) Smooth surface prepared with the small grain fraction. (b to d) Successive additions of large volcanic tuff grains on the smooth surface presented in Figure 1a. Figure 1b also illustrates the areas of the surface seen by the detectors at different emission angles. The circle in the center (2-cm diameter) corresponds to observations at nadir (emission angle = 0°). The three ellipses correspond to successive emission angles of 40°, 60° and 70° (from the smallest to the largest one).

[12] Surfaces were prepared carefully because the macroscopic texture (roughness) of the surface has a strong effect on the sample spectra and especially on reflectance variations between different measurement geometries [e.g., *Cord et al.*, 2003, 2005; *Shkuratov et al.*, 2005]. We prepared two ''smooth surfaces'' with the STx-1 smectite and the [50–100 μm] particle size fraction of the volcanic tuff. The sample holder was filled to rim with sample powder and then very slightly packed until the surface appeared perfectly smooth. As an example, a picture of the smooth surface prepared with the small grain volcanic tuff is presented in Figure 1a. To obtain different types of bidirectional reflectance distribution function (BRDF) behaviors, we initially prepared a smooth surface using the small grain volcanic tuff as already described, then added increasing quantities of large grains volcanic tuff on this smooth surface. This way of preparing surfaces is inspired by the results of *Johnson et al.* [2007]. Pictures of these surfaces are shown in Figure 1.

2.1.2. Reflectance Measurements

[13] All reflectance spectra were measured with the LPG Spectro-gonio-radiometer [*Brissaud et al.*, 2004]. This instrument is designed to measure reflectance spectra of particulate samples in the visible and near-infrared spectral range (0.3 – 4.8 μm) with a high degree of radiometric accuracy over wide angular ranges. All measurements presented in this paper are limited to maximum incidence and emergence angles of 70°. The azimuth angle was always fixed at 0°, that is, all measurements are in the principal plane. The effects of azimuth angle variations on the reflectance spectra may be investigated in future studies. The minimum phase angle at which measurements were made is 10°. Therefore none of our experimental measurements was affected by the narrow opposition effect that only affects reflectance a few degrees around opposition. To optimize experimental time, incidence and emergence angles were changed by steps of 10° which was sufficient to highlight the studied effects. The total time required to measure complete reflectance spectra (0.3–4.8 μm by steps of 0.02 μm) in all these geometrical configurations is very long (around one week). We acquired such measurements on long periods of time for the two smooth surfaces (smectite STx-1 and volcanic tuff). As atmospheric water content is susceptible to vary by large amounts over this period of time (following the diurnal temperature cycle and meteorological changes), we decided to perform these measurements in a closed cold room where temperature (−10°C) and atmospheric humidity are kept constant. All the other measurements were made on limited ranges of wavelength so that measurement times were shorter (a few hours) and it was acceptable to perform measurements under ambient laboratory conditions (air conditioned regulated at 25°C).

[14] The calibration of the samples reflectance spectra is performed by dividing each raw spectrum of the sample by the spectra of reference surfaces: commercial Spectralon® (Labsphere Inc.) for the 0.4–2.5 μm spectral range and Infragold® (Labsphere Inc.) for the 2.5–4.8 μm spectral range. Several corrections are applied to calibrate the bidirectional reflectance spectra with an absolute photometric accuracy better than 1% at all wavelengths and all geometrical configurations.

[15] Weak absorptions in the Spectralon® reflectance spectrum are corrected using data provided by Labsphere Inc. on the 0.4–2.5 μm spectral range. No spectral correction is applied to the Infragold reflectance spectrum as it is extremely flat over the 2.5–4.8 μm spectral range (data from Labsphere Inc.).

[16] Even if Spectralon® and Infragold® are qualified of "highly Lambertian" reference materials, calibrations of Spectralon® absolute BRDF conducted with the LPG spectro-gonio-radiometer [*Bonnefoy*, 2001] show that absolute errors up to 20% could be introduced for the geometrical conditions used in this study if these reference materials are assumed to be perfectly Lambertian. Therefore the uniform value of Spectralon® reflectance given by Labsphere Inc. is corrected for the Spectralon non-Lambertian behavior using absolute calibrations made on our own instrument [*Bonnefoy*, 2001]. The wavelength-independent reflectance values for the Infragold® surface are then calibrated relative to Spectralon® surface at 2.5 μm wavelength.

[17] The heterogeneity of the sample surface lightning also needs to be precisely known to allow for a correction of this artifact. This is done by using a small mobile detector scanning the entire illumination field of the sample surface. Surface illumination maps show a radial decrease of light intensity from the center to the periphery of the sample (relative variations of a few percents, see example on Figure 6 in the study of *Brissaud et al.* [2004]). This effect is corrected for each geometrical configuration by calculating the integrated illumination for observation ellipses corresponding to each emission angle and taking into account the effect of incidence angle variations (spreading of the illumination map along the principal plane).

[18] The curvature of the fiber optics varies as a function of the incidence angle inducing small illumination variations (Figure 5 in the study of *Brissaud et al.* [2004]). This effect generates absolute errors of 0.5 % in reflectance values. As our objective for this study was to obtain reflectance values with an absolute uncertainty lower than 1 % for all wavelengths and measurements geometrical conditions, it was not necessary to correct for this artifact. Therefore we retain 1 % as our absolute uncertainty in reflectance units for all measurements presented in this paper.

2.2. Radiative Transfer Numerical Modeling

2.2.1. Radiative Transfer Model

[19] We use the bidirectional reflectance model developed by *Douté and Schmitt* [1998] that calculates the radiative transfer of solar light through a dense granular medium. This model, on the basis of the theory of *Chandrasekhar* [1960], can be considered as an improvement of the widely used Hapke's model [*Hapke*, 1993]. In particular, analytical expressions are used for the multiple scattering terms contrasting with [*Hapke*, 1993] model where it is applied only on the first scattering term (multiple scattering is set isotropic). Anisotropy in the multiple diffusion terms was introduced latter, among other improvements, by *Hapke* [2002]. A discussion of differences between models proposed by *Hapke* [1993] and *Douté and Schmitt* [1998] can be found in the latter paper. The entries of the model are a set of free parameters that describe the properties of the individual particles, the dense granular medium made of these particles and the measurement geometry.

[20] Individual particles are characterized by their diameter, the intrinsic optical indices (n, k) of the material that constitutes the particles (see next section) and their scattering phase function. For all results presented in this study, the individual particle phase function is arbitrarily described by the classical Henyey-Greenstein form [*Henyey and Greenstein*, 1941] that is an analytical function of a single parameter: g ($g > 0$ for forward scattering particles and $g < 0$ for backscattering particles). It is important to note that we nominally use a constant value of the g parameter for all wavelengths. However, in some cases we calculate band strength parameters using reflectance values computed with different g values for the continuum and absorption band to illustrate differences induced by a wavelength-dependent g parameter.

[21] The narrow opposition effect resulting from both constructive interferences and shadow hiding effects a few degrees around phase angle = 0° [*Hapke*, 2002] is not modeled here. These effects are unlikely to appear in our measured spectra as 10° is the minimum phase angle used in all measurements.

[22] We construct libraries of synthetic spectra by varying by steps four free parameters (incidence angle, emergence angle, particle size and g parameter) to match as much as possible the parameters used in physical laboratory experiments (see previous part). These synthetic spectral libraries are calculated with a spectral sampling ($\sim$0.02 μm) and a spectral resolution similar to measured spectra.

[23] As the radiative transfer model is based on geometric optics physical laws, spectra of materials with very fine grains cannot be modeled. The longest wavelength used to calculate the 3-μm band strength being around 4 μm, we never calculate spectra with a particle size lower than 10 μm in order to keep the "optical size parameter", $x = \pi.D/\lambda$ in the valid range of geometrical optics.

2.2.2. Optical Constants

[24] The radiative transfer model we use requires the knowledge of the materials intrinsic optical constants (complex indices n and k). Proper extraction of optical indices from laboratory measured spectra is highly challenging. Therefore we did not try to determine the optical constants of our samples directly from our own laboratory measurements but decided to use the optical constants of the SWy-1 montmorillonite (Clay Mineral Society) published by *Roush* [2005]. This author proposes a new method to extract optical constants from laboratory measured reflectance spectra relying on a combination of scattering theory and Kramers-Kronig analysis. The main improvement of this method is the determination of wavelength-dependent real indices. This is a very important point as the real index (or refraction index n) is known to show large variations around strong fundamental absorption bands. As this is the case for the 3-μm band, it is crucial to use optical constants that correctly take this property into account.

2.3. Rationale for the Comparisons Between Measurements and Modeling

[25] As detailed in previous sections, both experimental and modeling approaches are used in this study. However, physical experiments and radiative transfer modeling are applied on different types of materials that differ by their chemistry, particle size and water content. These differences

between the materials prevent from direct comparisons between the absolute values of spectral criteria calculated from measured or calculated spectra. Thus only the relative trends between studied parameters can be compared.

[26] The objective of comparing measurements and modeling in this study is to obtain robust conclusions about the effects simultaneously observed on real samples in the laboratory and quantitatively described by the physical theory of radiative transfer. Robustness comes from the complementary advantages of the two different approaches. On one hand, laboratory experiments offer the ground truth that is often inaccessible on planetary surfaces and represent all the complexity of natural surfaces. On the other hand, it is always difficult to perfectly control all experimental conditions, especially when working with very volatile species like water. Radiative transfer modeling only offers approximations in all the relationships between the different parameters. However, the individual effects of all the parameters can be easily separated and studied.

2.4. Definition of Hydration Bands Spectral Criteria

[27] We calculate different spectral criteria to estimate the strength of the absorptions at 1.9 and 3 μm and to compare their behaviors under the effects of changes in incidence and emergence angles. The most common of these spectral criteria is the ''Band Depth'' defined by [*Clark and Roush*, 1984] as: $\mathrm{NBD}(l) = 1 - \frac{R(l)}{Rc(l)}$ where $R(\lambda)$ is the reflectance at the wavelength λ (usually the maximum of absorption) and $R_c(\lambda)$ is the value of a continuum defined above the absorption band at the same wavelength. This definition corresponds in fact to a ''Normalized Band Depth'' (relative to the continuum) and will be referred as ''NBD'' in the rest of this manuscript. This contrasts with the definition of ''Band Depth'' proposed by [*Morris et al.*, 1982] as a simple difference of reflectance between the band and the continuum: $\mathrm{BD}(\lambda) = R(\lambda) - R_c(\lambda)$.

[28] As the 3-μm water-of-hydration absorption band covers a large wavelength range, we also use integration criteria to estimate the strength of this band. We made the choice to integrate the 3-μm band between 2.9 μm and 3.8 μm to avoid absorption due to hydroxyl ions around 2.7 μm. On the right wing of the 3-μm band, 3.8 μm is the wavelength where reflectance is maximal on the majority of our samples. We calculated the Integrated Band Area (IBA) obtained by discrete integration of the difference between the continuum and the spectrum reflectance (BD) at each wavelength. IBA can then be normalized by the continuum reflectance to obtain the ''Normalized Integrated Band Area'' (NIBA). For all these criteria it is necessary to define a continuum above the absorption band to integrate its intensity. We have chosen to follow the definition of a flat continuum with a constant value as recommended by *Milliken and Mustard* [2007a, 2007b]. We tested different values for this continuum: the maximum of reflectance between 1 and 3 μm [*Milliken and Mustard*, 2007a, 2007b], the last local maximum in the continuum before the 3-μm absorption band (around 2.3 μm) or other points between 1 and 2.3 μm. Although absolute values of the spectral criteria can vary by a few percent according to the continuum definitions, we always obtain very similar results in terms of general relative trends when using these different values. Therefore we only present values calculated with a flat continuum equal to the value of the local reflectance maximum, around 2.3 μm, before the 3-μm absorption band. It must be noted that there is a small absorption by water at this wavelength. This is not problematic in this study because absorption is negligible compared to the 3-μm region but a definition of the continuum at 2.15 μm instead of 2.3 μm would be more appropriate for samples with lower water contents. This definition avoids taking into account an eventual slope in the near-infrared spectrum continuum that would not be linked with mineral hydration [*Fischer and Pieters*, 1993].

[29] The same criteria were also calculated from spectra converted from reflectance to apparent absorbance ($-\ln(R)$) and to single scattering albedo using equation 11.6 from [*Hapke*, 1993]. In this last case, we also calculated the ESPAT criterion from the single scattering albedo spectra using the formula proposed by [*Milliken and Mustard*, 2007a]. *Milliken and Mustard* [2005, 2007a, 2007b] propose the use of this spectral criterion to allow for the determination of minerals water content from their near-infrared spectra, independently of their nature, chemistry and albedo.

3. Results

3.1. Comparisons of Results for the Three Smooth Surfaces

3.1.1. Reflectance Spectra

[30] Figures 2, 3 and 4 present the bidirectional reflectance spectra measured or modeled under various illumination-observation configurations for three different materials with smooth surfaces. Figure 2 presents spectra of the STx-1 smectite (laboratory measurements), Figure 3 of the SWy-1 smectite (radiative transfer modeling) and Figure 4 of the volcanic tuff [50–100 μm] particle size fraction (laboratory measurements). The first order effect immediately visible on these plots is the ''forward scattering'' behavior of the three surfaces as the highest values of reflectance are observed for the highest phase angles. Second order spectral effects are also visible: reduction of the negative (blue) slope with respect to wavelength in the continuum of the STx-1 smectite at high phase angle (Figure 2) and pronounced positive (red) slope in the continuum of the volcanic tuff at high phase angle (Figure 4). On the contrary, modeled bidirectional spectra do not show any wavelength-dependant spectral effect when phase angle changes (Figure 3). This is a result of using a Henyey-Greenstein g parameter that is independent of wavelength for these calculations.

[31] The most interesting point concerning hydration bands is the behavior at the maximum of the absorption in the 3-μm absorption band (2.8–3.2 μm). Relative variations of reflectance in this range are extremely large at high phase angle, even if absorption is saturated and equal to 0 at low phase angle (case of the STx-1 smectite). This is due to the effect of the first external reflection on the particles (surface scattering) that becomes predominant at high phase angle whereas volume scattering was dominant at low phase angles.

3.1.2. BRDF in the Continuum

[32] BRDF polar plots offer a better visualization of the bidirectional scattering behavior of the three samples. On Figure 5, BRDF is plotted in polar coordinates at one single

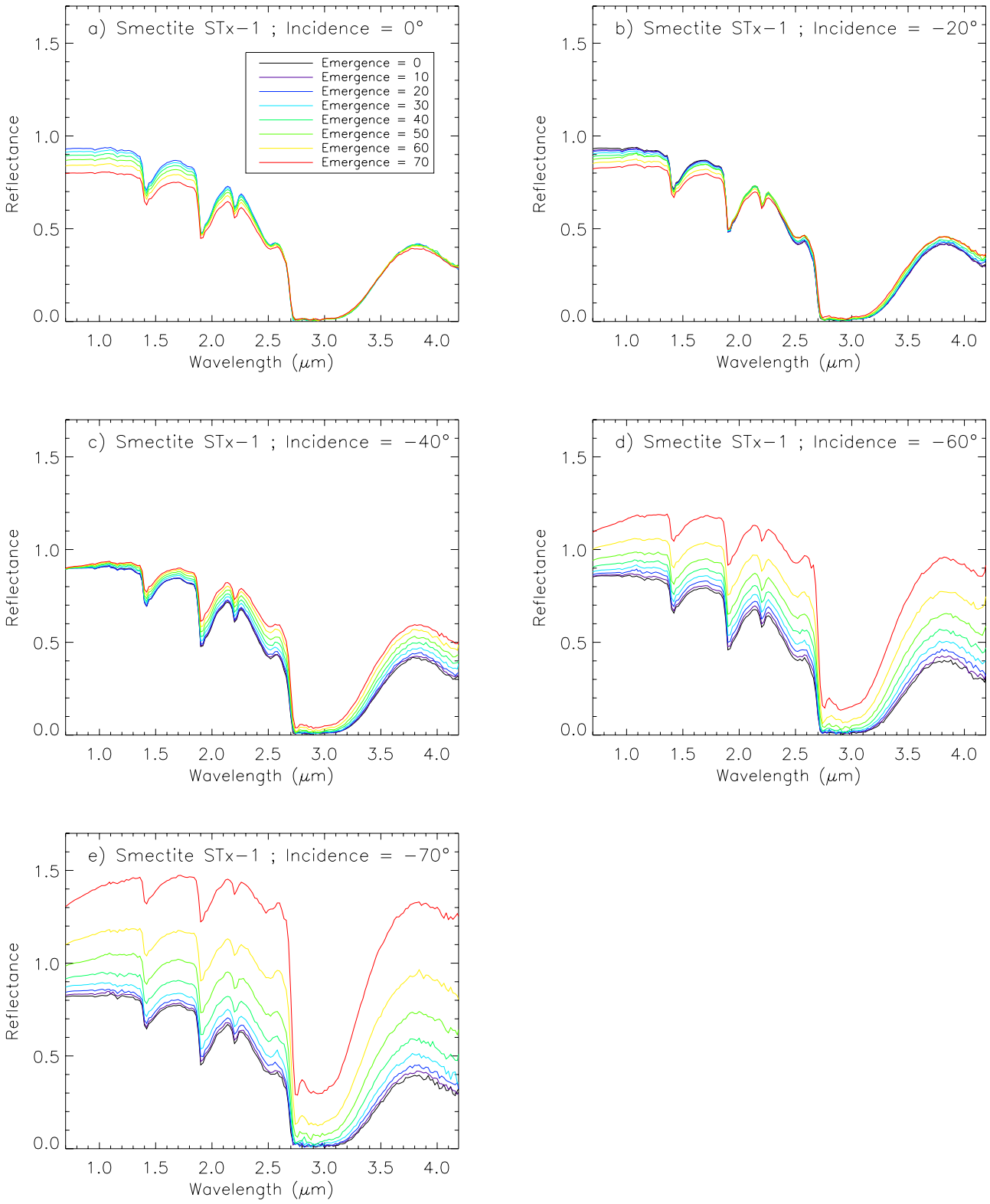

Figure 2. Bidirectional reflectance spectra of the STx-1 smectite (laboratory measurements). Each of the five plots presents spectra measured at a particular incidence angle (0°, 20°, 40°, 60° and 70°) but different emission angles (from 0° to 70°, see legend on Figure 2a).

wavelength (1.7 μm). This wavelength was chosen because it is situated in the continuum of the three samples spectra and thus is not affected by absorption. Smectite STx-1 and volcanic tuff (both measured) present relatively similar behaviors of the BRDF but scattering in the forward direction is slightly more intense in the case of the volcanic tuff. The BRDF behavior of the model smectite SWy-1 depends both on the values of particle size, d and Henyey-

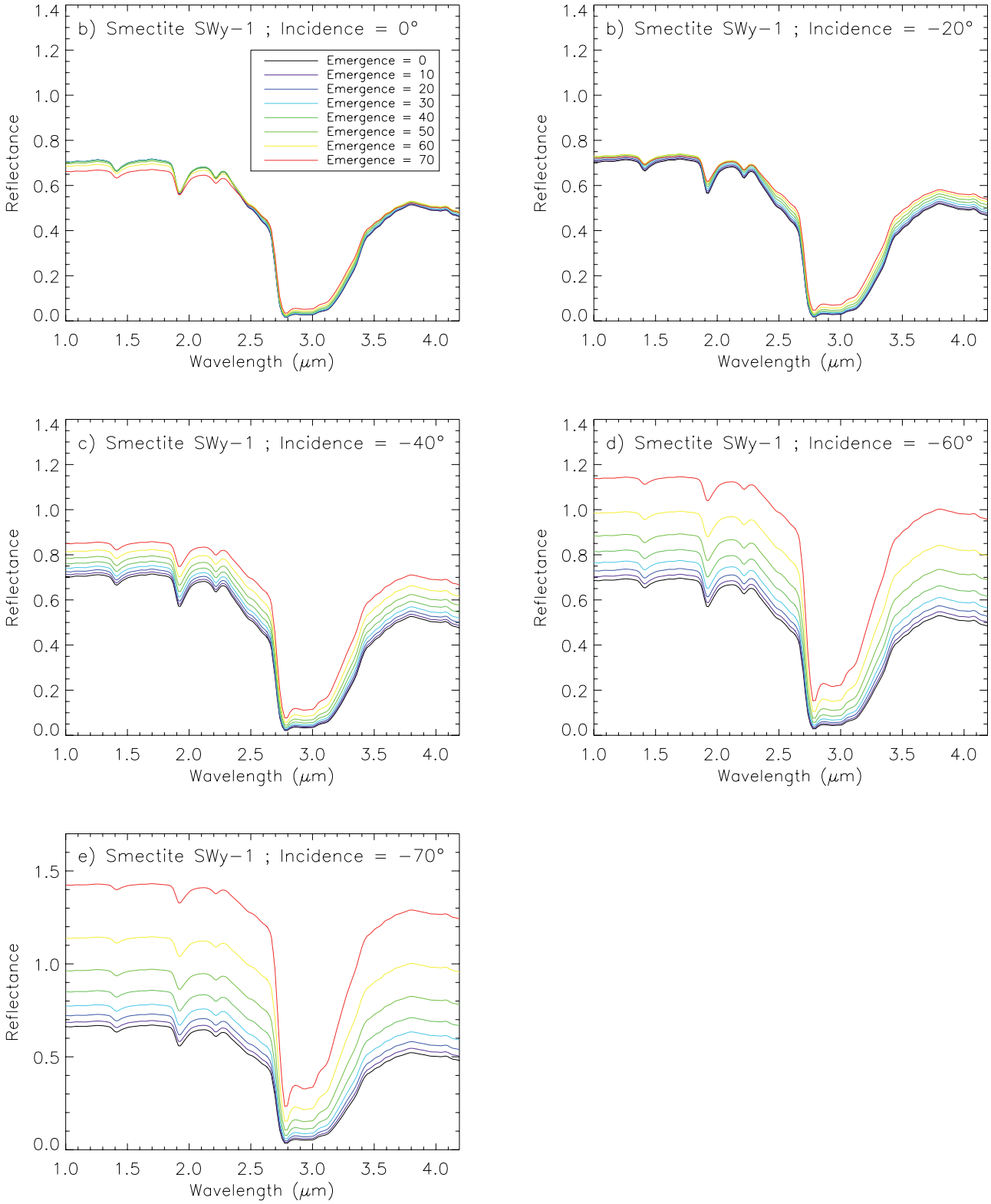

Figure 3. Bidirectional reflectance spectra of the SWy-1 smectite. Spectra modeled with a particle diameter: d = 20 μm and an anisotropy parameter: g = 0.4. Each of the five plots presents spectra measured at a particular incidence angle (0°, 20°, 40°, 60° and 70°) but different emission angles (from 0° to 70°, see legend on Figure 3a).

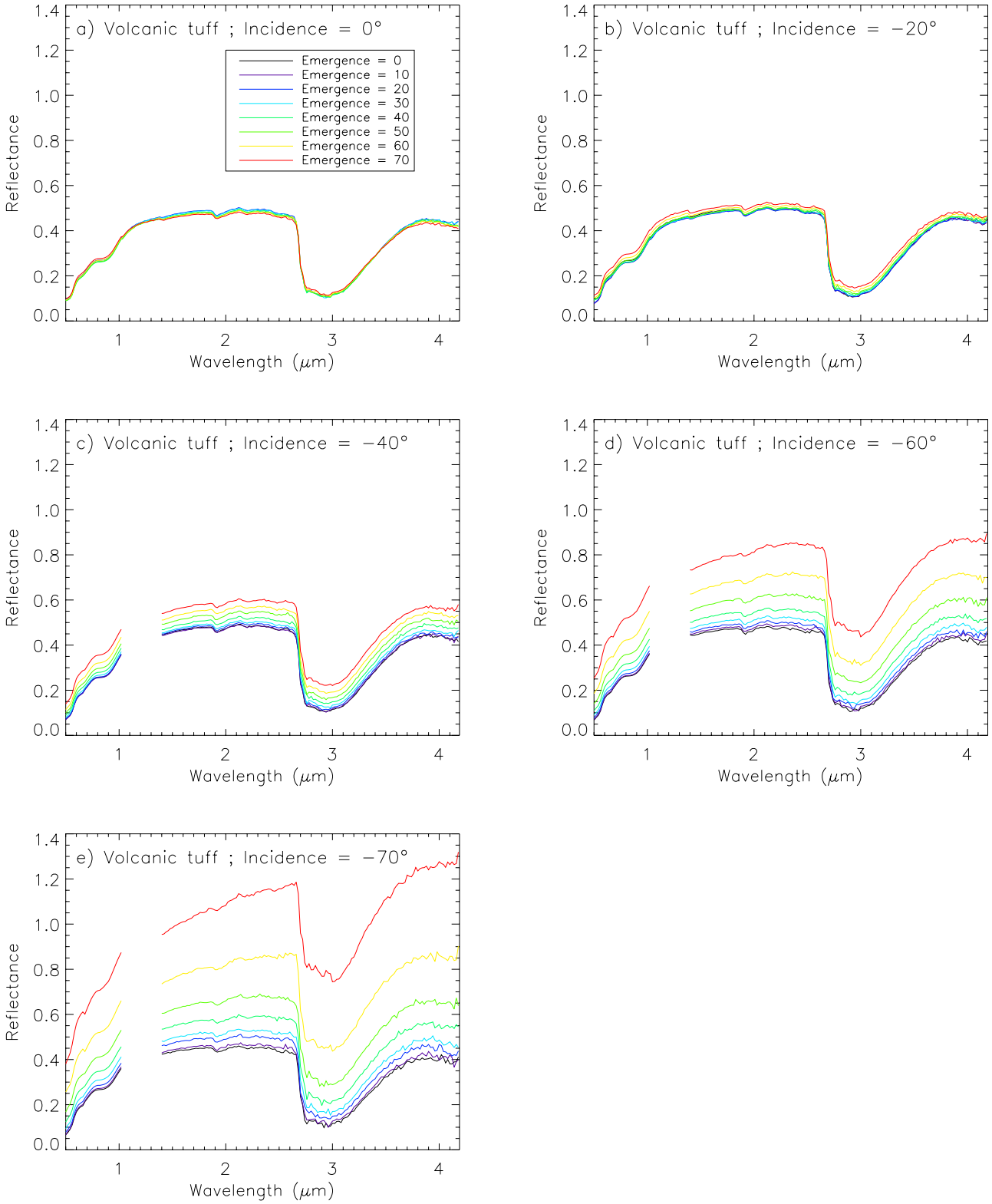

Figure 4. Bidirectional reflectance spectra of the volcanic tuff (50–100 μm) particle size fraction (laboratory measurements). Each of the five plots presents spectra measured at a particular incidence angle (0°, 20°, 40°, 60° and 70°) but different emission angles (from 0 to 70°, see legend on Figure 4a).

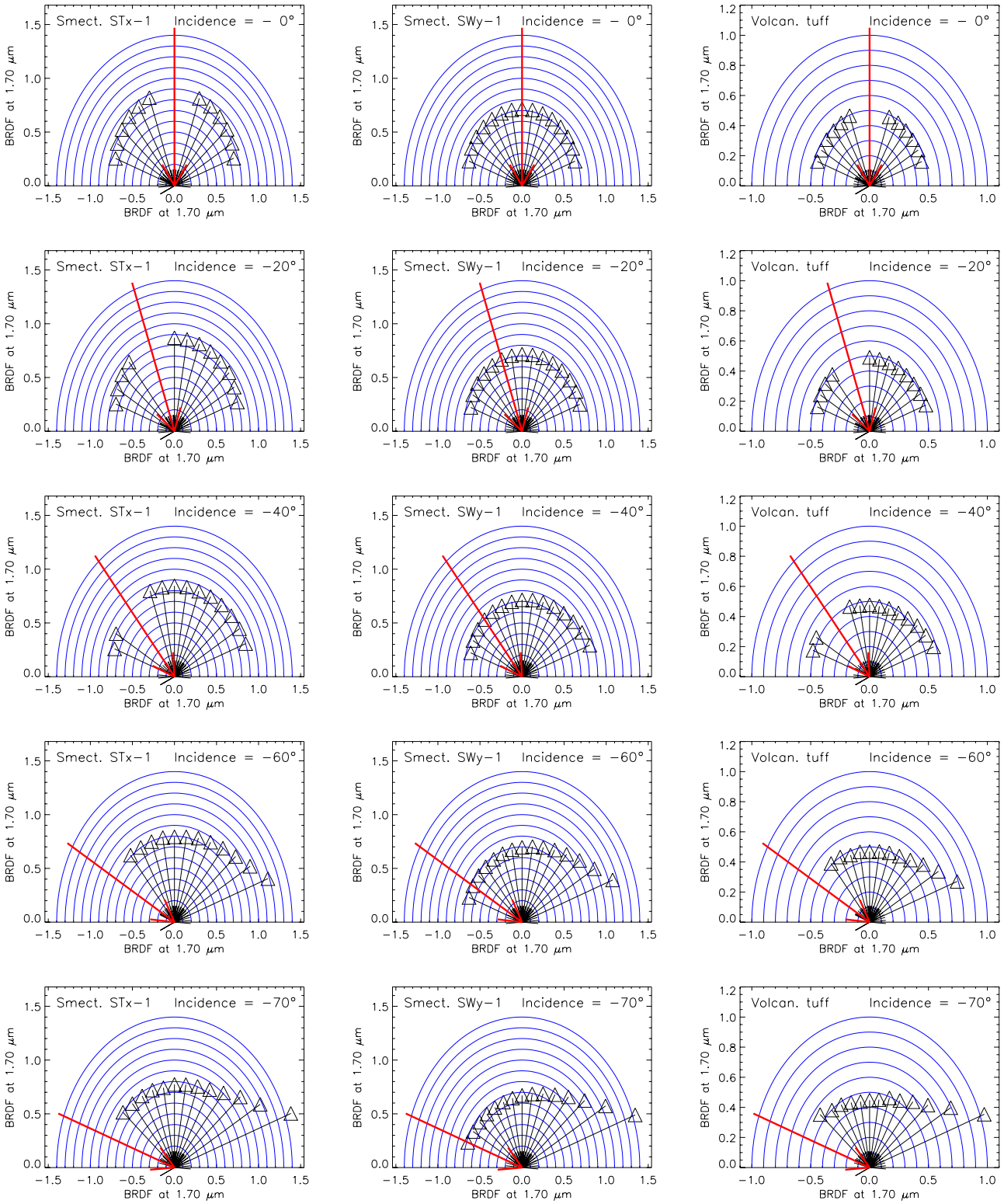

Figure 5. BRDF polar plots for the three smooth surfaces. BRDF is plotted at 1.70 μm, in the spectra continuum for all samples. (left column) Smectite STx-1 (laboratory measurements). (center column) Smectite SWy-1 (model with a particle diameter: $d = 20$ μm and an anisotropy parameter: $g = 0.4$). (right column) Volcanic tuff (laboratory measurements). Each row corresponds to a different incidence angle (0°, 20°, 40°, 60°, 70° from top to bottom). Semicircles indicate iso-values of BRDF by steps of 0.1. These three surfaces all show a strong forward scattering behavior in the continuum.

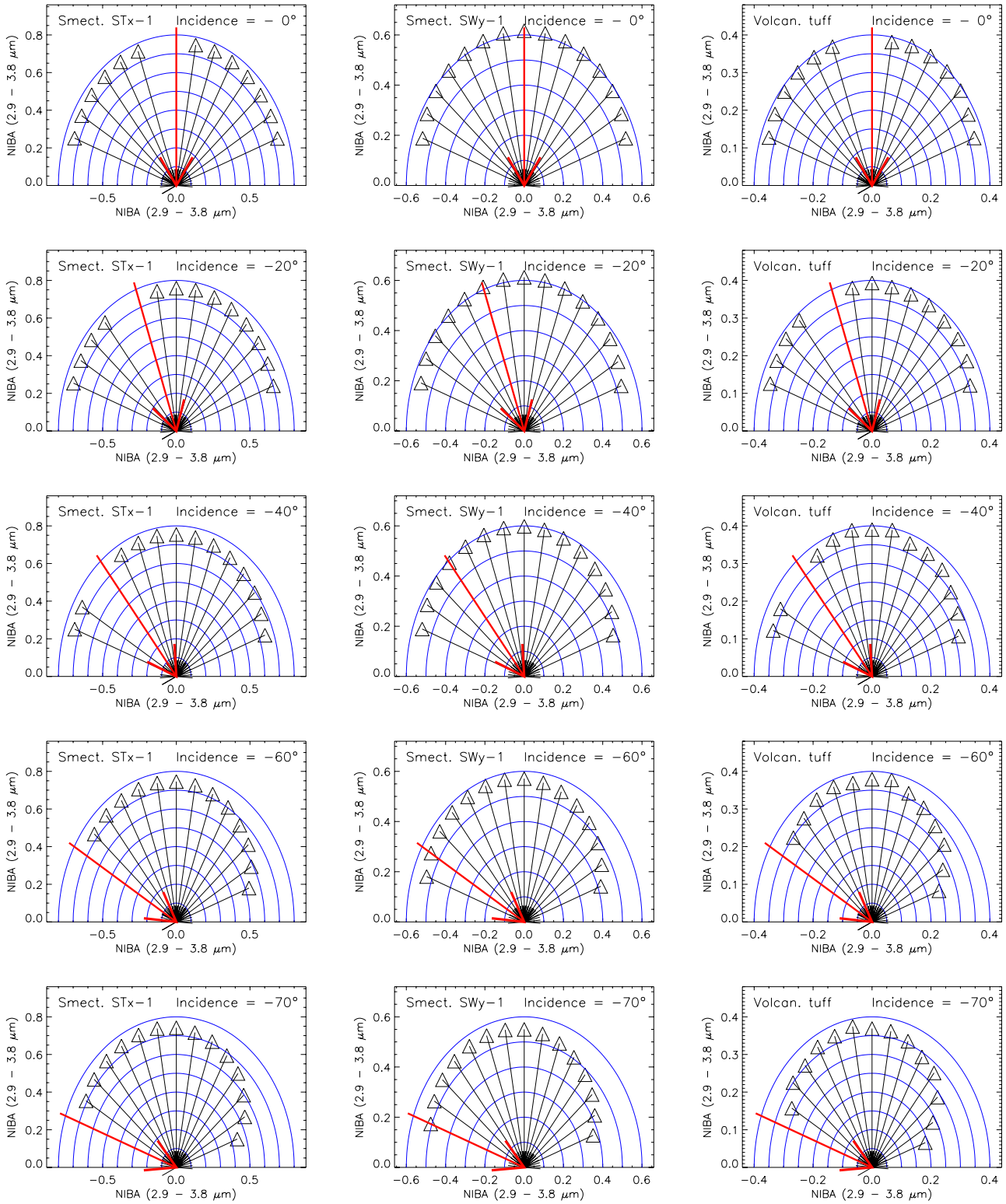

Figure 6. Polar plots of the 3-μm band NIBA parameter values calculated for the three materials prepared as smooth surfaces. (left column) Smectite STx-1 (laboratory measurements). (center column) Smectite SWy-1 (model with d = 20 μm and g = 0.4). (right column) Volcanic tuff (laboratory measurements). Each row corresponds to a different incidence angle (0°, 20°, 40°, 60°, 70° from top to bottom).

Greenstein parameter, g. Influence of these parameters is studied later in this manuscript. For calculations presented in Figure 5, we fixed $d = 20$ μm and $g = 0.4$. These values result in good correspondence between calculated (SWy-1) and measured (STx-1) reflectivities at high phase angles. At first order, the shape of the BRDF in the continuum is consistent between measurements and modeling.

3.1.3. H_2O Bands Strength

3.1.3.1. Polar Plots of Band Strength

[33] We represent the behaviors of spectral criteria designed to estimate the strength of hydration bands in polar coordinates as this was done for BRDF in the continuum in Figure 5. The different spectral criteria defined in section 2 were calculated from all measured and modeled spectra. However, to save place, we only plot NIBA for the 3-μm band and NBD for the 1.9-μm band. Variability of behaviors associated with the different definitions of the spectral criteria will be studied in next section.

[34] Values of the Normalized Integrated Band Area (NIBA) calculated between 2.9 and 3.8 μm for the three samples are presented in polar coordinates for different incidence and emergence angles on Figure 6. All these plots show that the first order effect of measurement geometry variations is a decrease of the NIBA value for the highest values of phase angle while values of NIBA look relatively independent from measurement geometry at lower phase angles. Normalized Band depth (NBD) calculated between a wavelength in the continuum and a wavelength in the band shows the same behavior as NIBA (not plotted). The shape looks similar for the three samples but relative variations of NIBA between two different viewing conditions appear a little bit more pronounced for the volcanic tuff than for the smectite STx-1. This is in agreement with BRDF behavior in the continuum, as forward scattering appeared more pronounced for the volcanic tuff than for the smectite. As in previous figures, results from modeling (Smectite SWy-1) presented on Figure 6 were obtained with a particle size of 20 μm and a scattering anisotropy parameter $g = 0.4$. Results from modeling and measurements are consistent for the smectites.

[35] The same representation is adopted for Normalized Band Depth (NBD) at 1.9 μm (Figure 7). This spectral criterion is only calculated for the two smectites because this band is too weak in volcanic tuff spectra. As observed for NIBA at 3 μm, a strong decrease of NBD occurs for the largest phase angles but NBD at 1.9 μm shows larger relative variations between different geometries at lower phase angles than NIBA at 3 μm.

3.1.3.2. Comparison of BRDF in the Continuum and the Absorption Bands

[36] To explain the observed variations of band strength versus measurement geometry, we plot together values of reflectance in the continuum before the absorption band and in the middle of the absorption band. To allow for a direct comparison between the BRDF behaviors at these wavelengths, we normalize the two BRDF sets by the maximum value at each wavelength. Figure 8 presents these plots for the 3-μm band (continuum at 2.26 μm and absorption band at 3.4 μm) while Figure 9 presents similar plots for the 1.9-μm band (continuum at 1.80 μm and absorption band at 1.92 μm).

[37] For both the 1.9-μm and 3-μm bands, the same effect is clearly visible. BRDF in the absorption band is more strongly forward scattering than BRDF in the continuum. Therefore, when phase angle increases, reflectance in the absorption band increases by a larger amount than reflectance in the continuum. This implies a reduction of contrast between absorption band and continuum and a corresponding decrease in band strength.

[38] An important discrepancy between results for laboratory experiments (STx-1 smectite) and radiative transfer modeling (SWy-1 smectite) can be observed both for the 1.9 and the 3-μm bands. BRDF in the continuum and in the absorption band are more similar in the models. This contrasts with experimental results showing very different behaviors of BRDF in the continuum and in the absorption band. Two effects can contribute to this discrepancy. First, absorptions at 1.9 and 3.4 μm are weaker for the SWy-1 smectite (modeling) than for the STx-1 smectite (measurements), thus reducing the contrast of BRDF behaviors between the continuum and the absorption band in the case of the SWy-1 smectite. However, the major contribution to this discrepancy is more probably the choice of a constant Henyey-Greenstein parameter g. A better consistency with experimental results would be obtained by choosing a larger g parameter in the band than in the continuum. This particular point is illustrated and discussed later in this paper.

[39] The strongly enhanced forward scattering behavior in the absorption band compared to the continuum may seem counterintuitive at first view: at high incidence angle, the amount of light transmitted through the grains in the forward direction decreases as absorption increases. However, the relative contribution of single scattering on particles' external surfaces becomes predominant for high absorption values and gives to the BRDF its forward scattering behavior due to the large reflection coefficients at high incidence angles. This effect is also highlighted for isolated irregular particles using Monte-Carlo methods [*Grundy et al.*, 2000].

3.1.3.3. Band Strength Versus Phase Angle

[40] Figure 10 presents Normalized Band Depth (NBD) at 3.2 μm and Normalized Integrated Band Area, both calculated from reflectance spectra plotted as a function of phase angle for the STx-1 and SWy-1 smectites (respectively measured and modeled) and the volcanic tuff [50–100 μm] particle size fraction (measured). Series of data corresponding to the same incidence angle are distinguished by the use of different symbols. It is clear from the plots that phase angle is the key parameter that controls variations of band strength linked to variations of measurement geometry. For a given value of phase angle, variability is very small among measurements made with different incidence or emergence angles and is only significant at low phase angles.

[41] Criteria calculated from reflectance spectra (Figures 10a to 10d) remain almost constant for phase angles lower than about 80°. However, for larger phase angles, BD and NIBA strongly decrease. Relative variation of NIBA between 80° and 140° is 40% for the STx-1 smectite and 70% for the volcanic tuff. The difference between these two samples could be expected from the BRDF polar plots (Figure 5) as the volcanic tuff surface displays a more

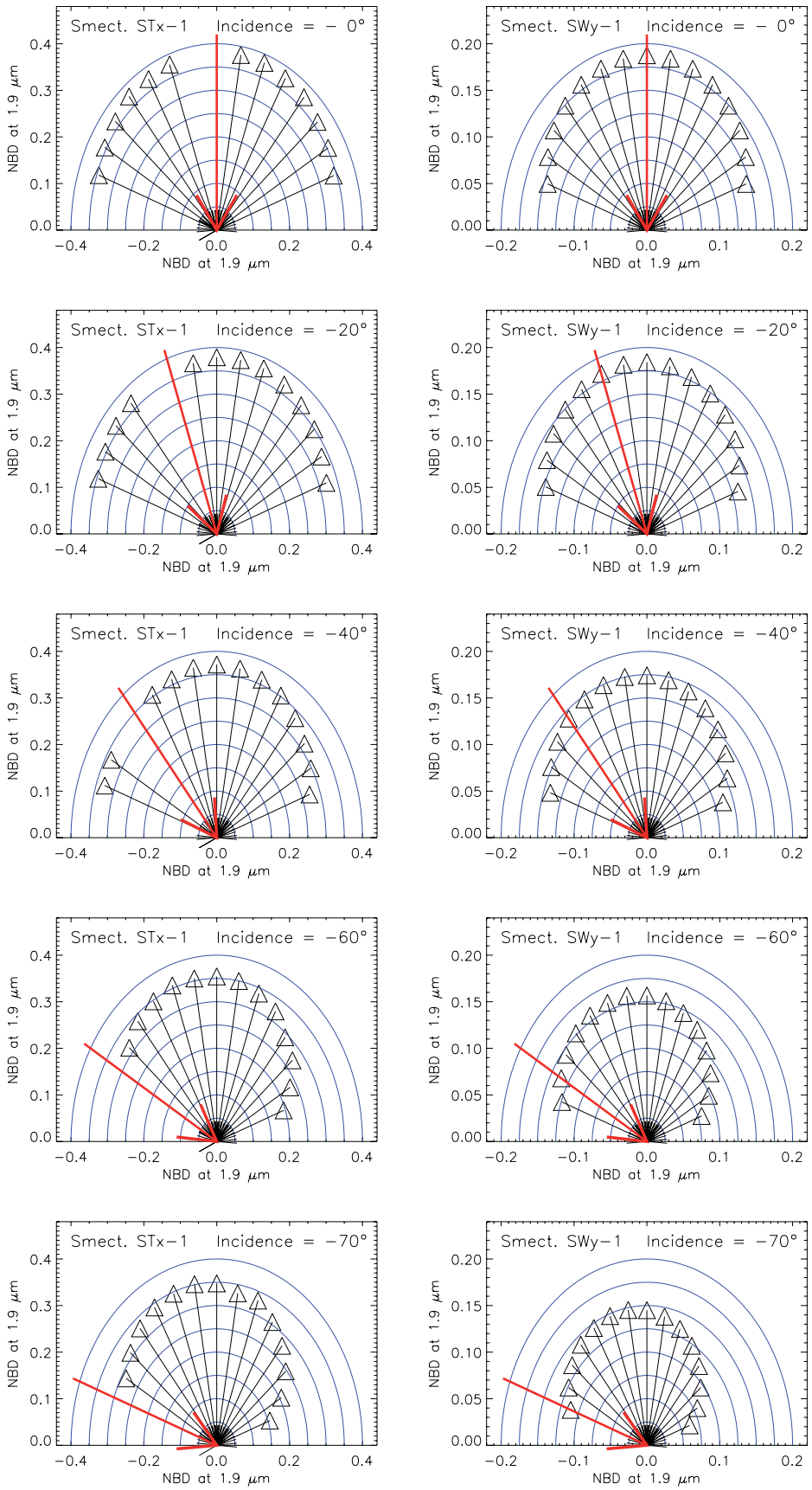

Figure 7. Polar plots of the 1.9-μm band NBD parameter values calculated for the two smectites. (left column) Smectite STx-1 (laboratory measurements). (right column) Smectite SWy-1 (model with $d = 20$ μm and $g = 0.4$). Each row corresponds to a different incidence angle (0°, 20°, 40°, 60°, 70° from top to bottom).

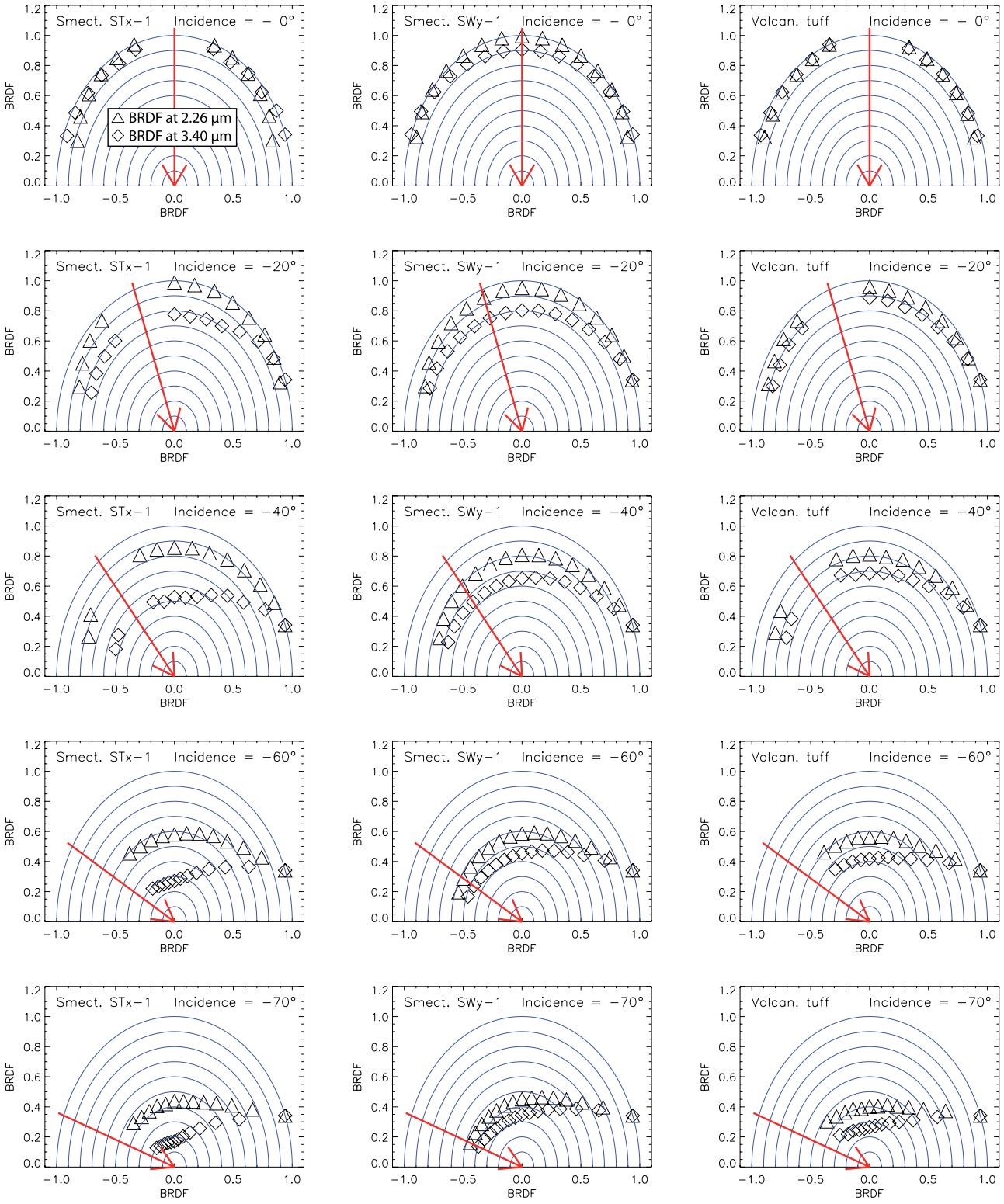

Figure 8. BRDF polar plots for the three smooth surfaces. BRDF is plotted at two different wavelengths: 2.26 μm (continuum) and 3.4 μm (in the middle of the 3-μm absorption band). To allow for a better comparison between the BRDF shapes, BRDF at each wavelength is normalized by its maximum value. (left column) Smectite STx-1 (laboratory measurements). (center column) Smectite SWy-1 (model with d = 20 μm and g = 0.4). (right column) Volcanic tuff (laboratory measurements). Each row corresponds to a different incidence angle (0°, 20°, 40°, 60°, 70° from top to bottom).

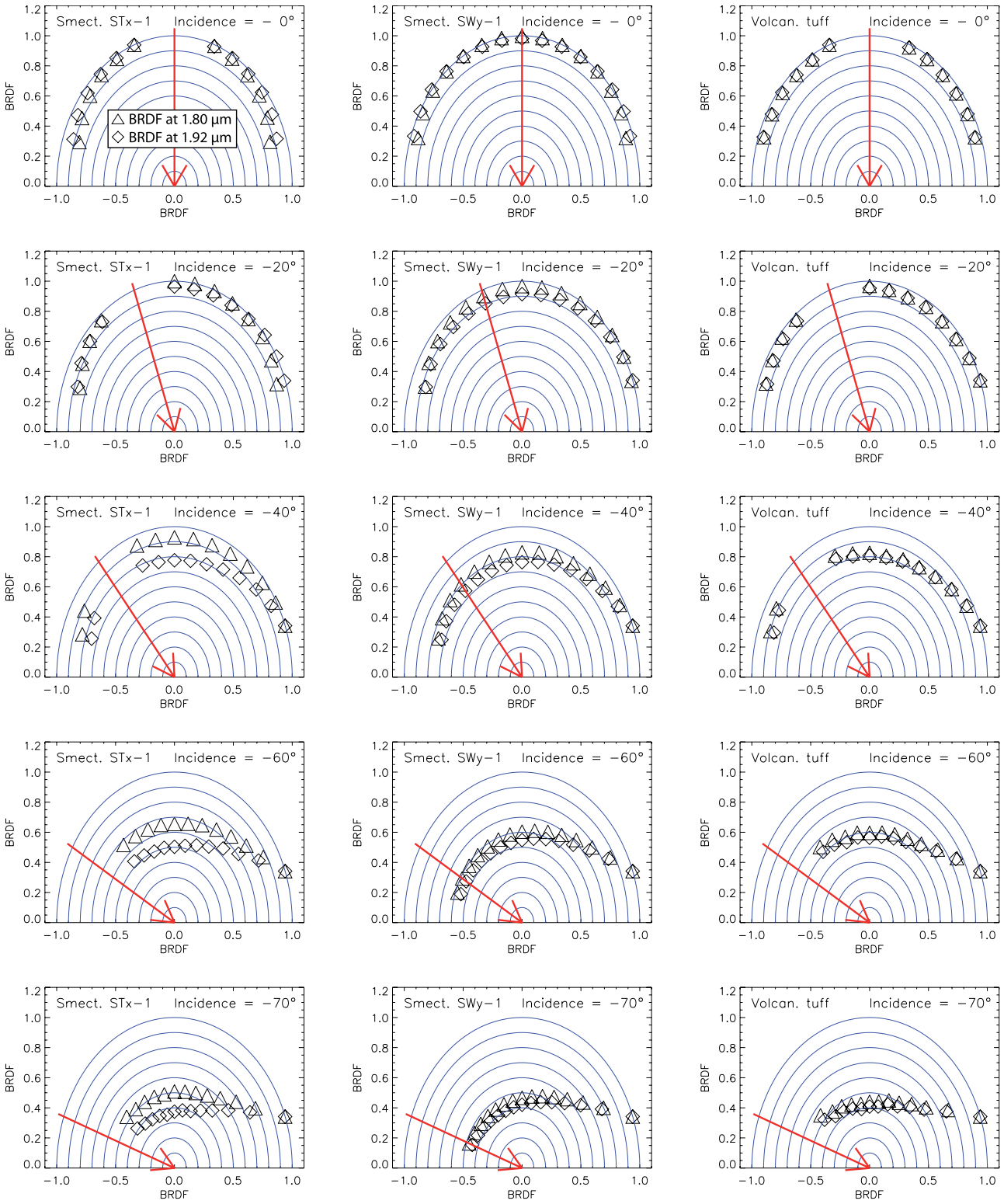

Figure 9. BRDF polar plots for the three smooth surfaces. BRDF is plotted at two different wavelengths: 1.80 μm (continuum) and 1.92 μm (minimum in the 1.9-μm absorption band). To allow for a better comparison between the BRDF shapes, BRDF at each wavelength is normalized by its maximum value. (left column) Smectite STx-1 (laboratory measurements). (center column) Smectite SWy-1 (model with d = 20 μm and g = 0.4). (right column) Volcanic tuff (Laboratory measurements). Each row corresponds to a different incidence angle (0°, 20°, 40°, 60°, 70° from top to bottom).

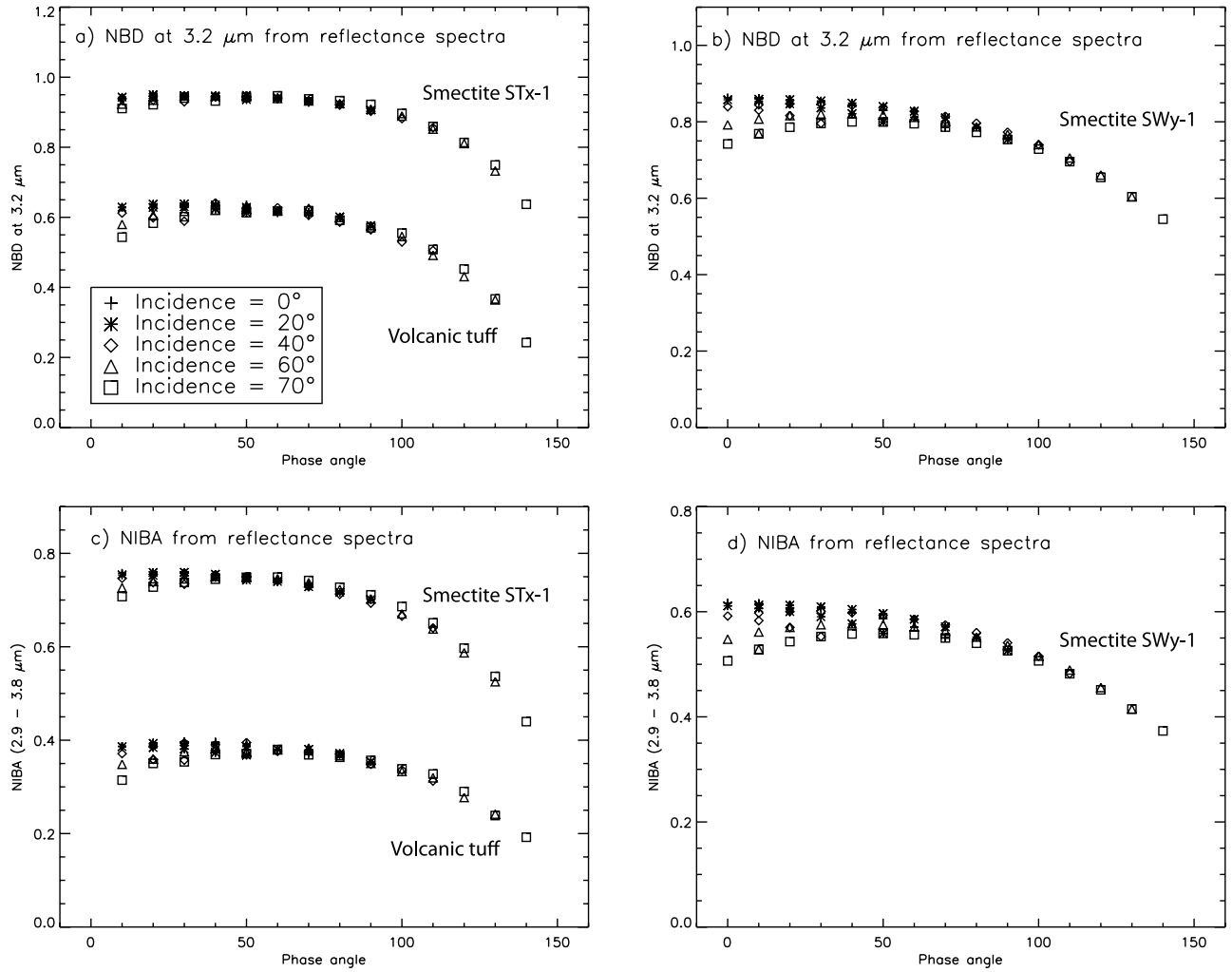

Figure 10. Evolution of the 3-μm band strength as a function of phase angle. (a and c) Experimental results for the STx-1 smectite (top trace in each plot) and the volcanic tuff (bottom trace). (b and d) Results from radiative transfer modeling for the SWy-1 smectite (d = 20 μm and g = 0.4). Different symbols are used to distinguish series of measurements made with different incidence angles (see legend on Figure 10a).

pronounced ''forward scattering'' behavior than the smectite surface. Except the amplitude of relative variations, the relationship between band strength and phase angle is the same for the smectite and the volcanic tuff even if the 3-μm band is partly saturated in the case of the STx-1 smectite whereas it is never saturated in the case of the altered volcanic tuff.

[42] Radiative transfer modeling produces the same kind of behaviors (Figures 10b and 10d). On closer inspection, discrepancies can be seen. At low phase angle, variability of the values is larger whereas at high phase angle relative decrease of band strength is smaller compared to measurements. The general shape of the relationship between band strength and phase angle is also different. Model band strength continuously decreases when phase angle increases whereas the same quantities calculated from measured spectra remain constant at phase angle lower than 80°. As discussed previously, those discrepancies are probably due to the use of a Henyey-Greenstein g parameter that is independent of wavelength in the model. This hypothesis is tested in the following section.

[43] Figure 11 presents the same relationships as Figure 10 but established with other spectral criteria calculated following the definitions presented in section 2. IBA calculated from reflectance spectra (Figures 10a and 10b) present similar relationship to phase angles for both measured and modeled smectite. At low phase angle, variability is relatively high for different values of incidence and emergence. At phase angle larger than about 100°, IBA values increase as a function of phase angle. Relative variations are comparable for NBD or NIBA. In contrast, IBA calculated from reflectance spectra of the volcanic tuff show only very limited variations versus phase angle. The main difference between smectites and volcanic tuff is the absolute intensity of the absorption that is partly saturated or almost saturated in the 3-μm region for the smectite whereas the band is always far from saturation in the case of the volcanic tuff. IBA values calculated from apparent absorbance spectra

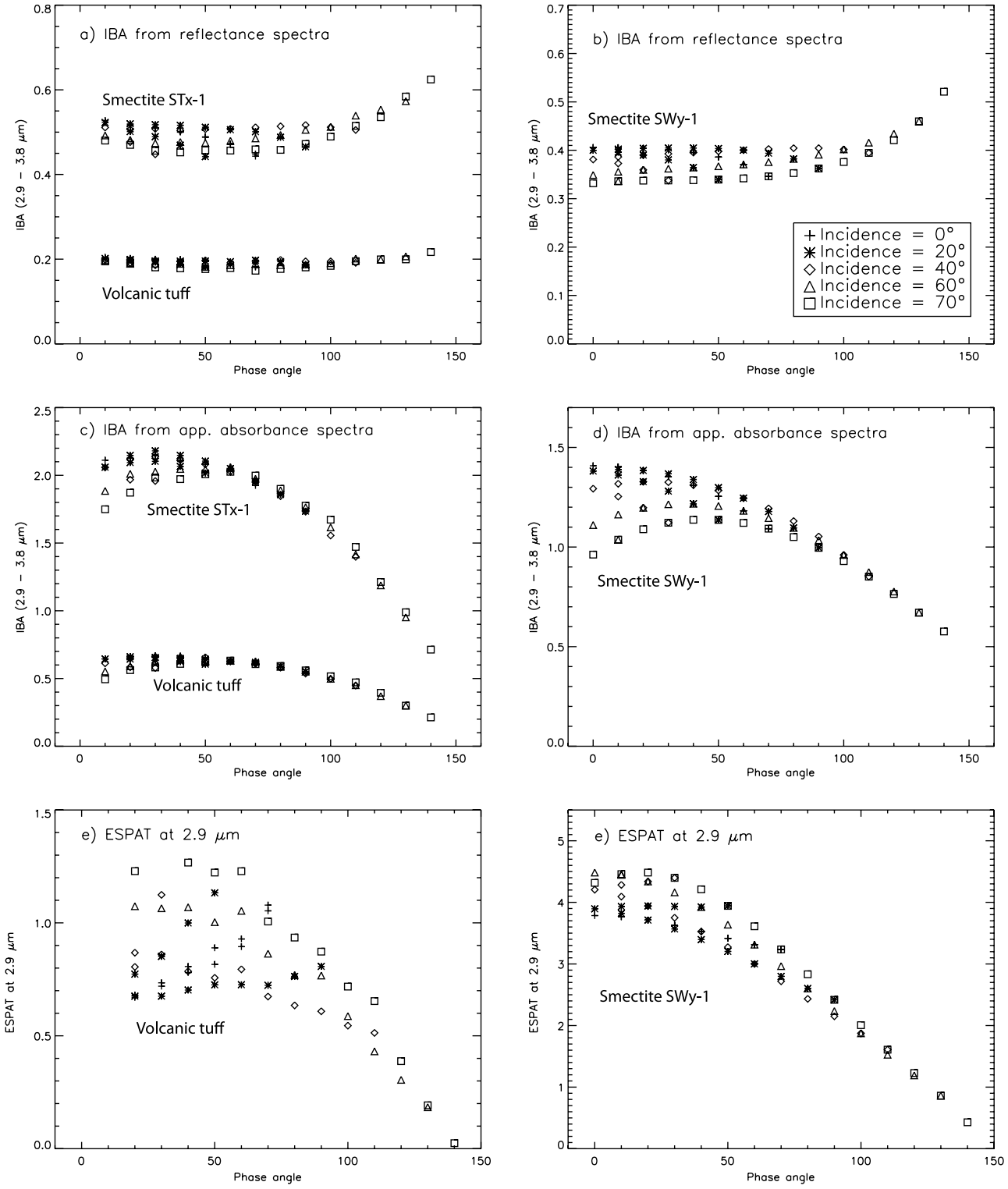

Figure 11. Same as Figure 10 but using different spectral criteria to estimate the strength of the 3-μm band. (a and c) Experimental results for the STx-1 smectite (top trace in each plot) and the volcanic tuff (bottom trace). (e) Experimental results for the volcanic tuff only. (b, d and f) Results from radiative transfer modeling for the SWy-1 smectite (d = 20 μm and g = 0.4).

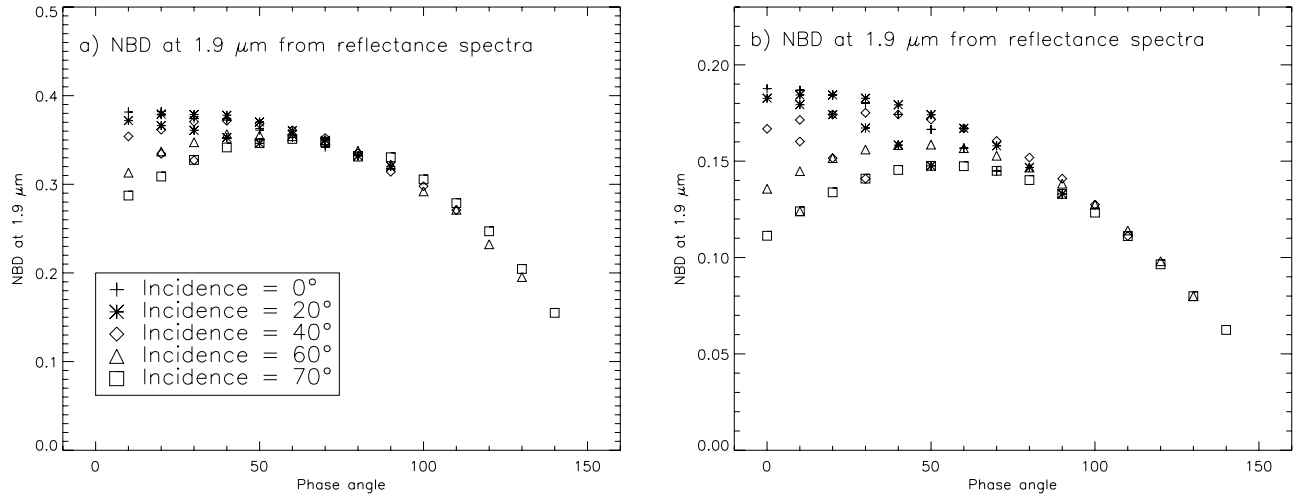

Figure 12. Evolution of the 1.9-μm Normalized Band Depth (NBD) as a function of phase angle. (a) Experimental results for the STx-1 smectite. (b) Results from radiative transfer modeling for the SWy-1 smectite (d = 20 μm and g = 0.4). Different symbols are used to distinguish series of measurements made with different incidence angles (see legend on Figure 12a).

(Figures 10c and 10d) display strong variations versus phase angles in the case of smectites. Relative variations between high and low phase angles are enhanced compared to criteria calculated from reflectance spectra and variability at low phase angle is larger. In the case of the volcanic tuff, IBA calculated from apparent absorbance gives similar results to NBD or NIBA calculated form reflectance spectra. Absolute intensity of the 3-μm band is again the major cause of differences between smectite and volcanic tuff. Finally, we calculated ESPAT at 2.9 μm from spectra converted to single scattering albedo as defined by *Milliken and Mustard* [2005]. Values of this criterion show very large variations versus phase angle. This is chiefly due to the assumption of a Lambertian scattering behavior used in the conversion from reflectance to single scattering albedo.

[44] Figure 12 presents the evolution of the 1.9-μm band strength as a function of phase angle for the STx-1 smectite (measurements) and SWy-1 smectite (modeling). Only Normalized Band Depth (NBD) criterion calculated from reflectance spectra is plotted. The main difference with the case of the 3-μm band is that the 1.9-μm band strength decreases when phase angle increases even for low phase angles whereas the 3-μm band strength remains constant up to about 80°. The other difference is that data for a same phase angle but different incidence or emergence angles show more variability. This is evident both from measurements and models. The relative variations of band strength between low and high phase angles are of the same order of magnitude as observed for the 3-μm band: Band Depth calculated on reflectance spectra decreases by a factor of 2.5 when phase angle varies from 10° to 140°.

3.1.4. Numerical Modeling With a Wavelength-Dependant *g* Parameter

[45] In the case of radiative transfer modeling, the most important free parameter regarding this study is the Henyey-Greenstein scattering anisotropy parameter, g. We calculated reflectance spectra of the SWy-1 smectite using different, but constant, values (from 0 to 0.8 by steps of 0.1, no wavelength-dependence) of this parameter for each simulation. However, as already discussed, this assumption is the cause of many discrepancies between the model and experimental results. Especially, it is evident from experimental results that scattering anisotropy is far stronger in the band than it is in the continuum (Figures 8 and 9), which is not correctly handled by the model. The discrepancies between experimental results and results from the model evident in Figure 11 are also attributed to that cause. To test this hypothesis, we calculated NBD in the 3-μm band using different values of the g parameter for the continuum and the absorption band. The parameter g was kept constant in the continuum: g = 0.2 while it was allowed to vary between 0.2 and 0.6 at the bottom of the absorption band. Values of NBD at 3.2 μm are plotted versus phase angle in Figure 13. When g(3.20 μm) increases, variations at low phase angles are reduced (Figures 13a to 13d) compared to the case where g(3.20 μm) = g(2.26 μm) = 0.2 (Figure 13a). Furthermore, when g(3.20 μm) increases, relative variations of NBD between phase angles 0 and 80° decrease whereas relative variations between phase angles 80 and 140° increase. Therefore the main discrepancies noted between results from experiments and modeling (Figure 11) seem to disappear when a larger value of g is used for the absorption band than for the continuum.

3.2. Surfaces Covered With Millimeter-Scale Grains

[46] Figure 1 presents macroscopic pictures of four different surfaces prepared with the volcanic tuff [50–100 μm] and [800–1120 μm] particle size fractions by adding increasing amounts of large grains on the smooth surface prepared with the small grains (results for this smooth surface have been extensively presented in previous sections). All different particle size fractions are obtained by grinding from a unique initial material. Therefore the different fractions are expected to have the same composition. For each of these four surfaces, BRDF at 1 μm was measured to study the transition from a forward scattering to a backscattering behavior. Polar plots of BRDF at 1 μm are presented on Figure 14. The expected behavior of the

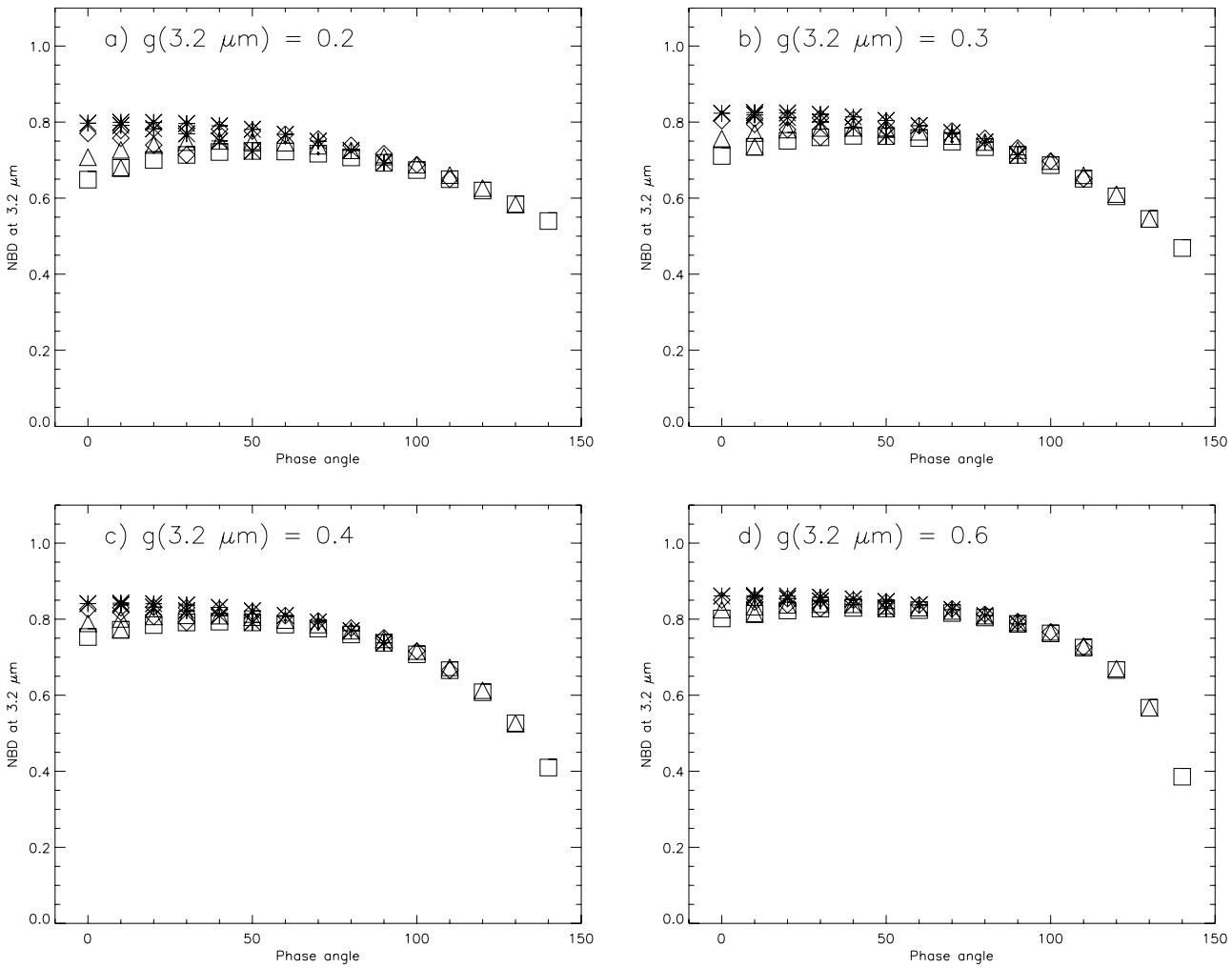

Figure 13. Illustration of the effects of the spectral variations of the scattering anisotropy parameter on the relationship between band strength and measurement geometry established by radiative transfer modeling. These four plots show NBD at 3.2 μm versus phase angle for the SWy-1 smectite. Particle size is kept constant at 20 μm. Reflectance at 2.26 μm (continuum for the 3-μm absorption band) is modeled with a constant anisotropy parameter $g = 0.2$. Reflectance at 3.2 μm is modeled with a variable anisotropy parameter (increasing from 0.2 to 0.6, Figures 13a to 13d).

BRDF is easily observed. As large grains are added to the smooth surface, BRDF decreases at high phase angles while reflectance back in the direction of the incident light increases. This is due to the effect of shadows projected by large grains that reduce the area that receives incident light when incidence angle increases. The aim of this simple experiment is to study the behavior of the 3-μm absorption band strength when the surface becomes backscattering. Therefore BRDF at a wavelength inside the 3-μm band (3.2 μm) was also measured for surfaces 3 and 4 so that the evolution of Normalized Band Depth at 3.2 μm versus measurement geometry can be compared with the one previously obtained for the smooth small grains surface. Figure 15 presents polar plots of Normalized Band Depth (NBD) measured at 3.2 μm for the three surfaces.

[47] These plots look very similar for the three different surfaces at each incidence angle. The only obvious difference is a reduced decrease in Normalized Band Depth at high phase angles for surfaces with increasing amount of large grains. If we look at the evolution of BRDF at the two wavelengths (continuum and central band) used to calculate NBD (Figure 16), it is evident that both continuum reflectance and reflectance in the band show strong differences in their angular behavior from one sample to another.

[48] However, calculation of NBD normalizes these differences and indicates the same angular behavior of band strength for all these surfaces, independent of their scattering behavior.

[49] This is even more obvious when Normalized Band Depth at 3.2 μm is plotted versus phase angle for all measurements (Figure 17). The evolutions of NBD versus phase angle look the same except a larger variability of values for surfaces partially covered with large grains that can be explained by the heterogeneous nature of the surface. When the observation angle is changed, the surface seen by the detector is different (see Figure 1b for an illustration) and the ratio between areas covered by small and large grains can be slightly different introducing a small disper-

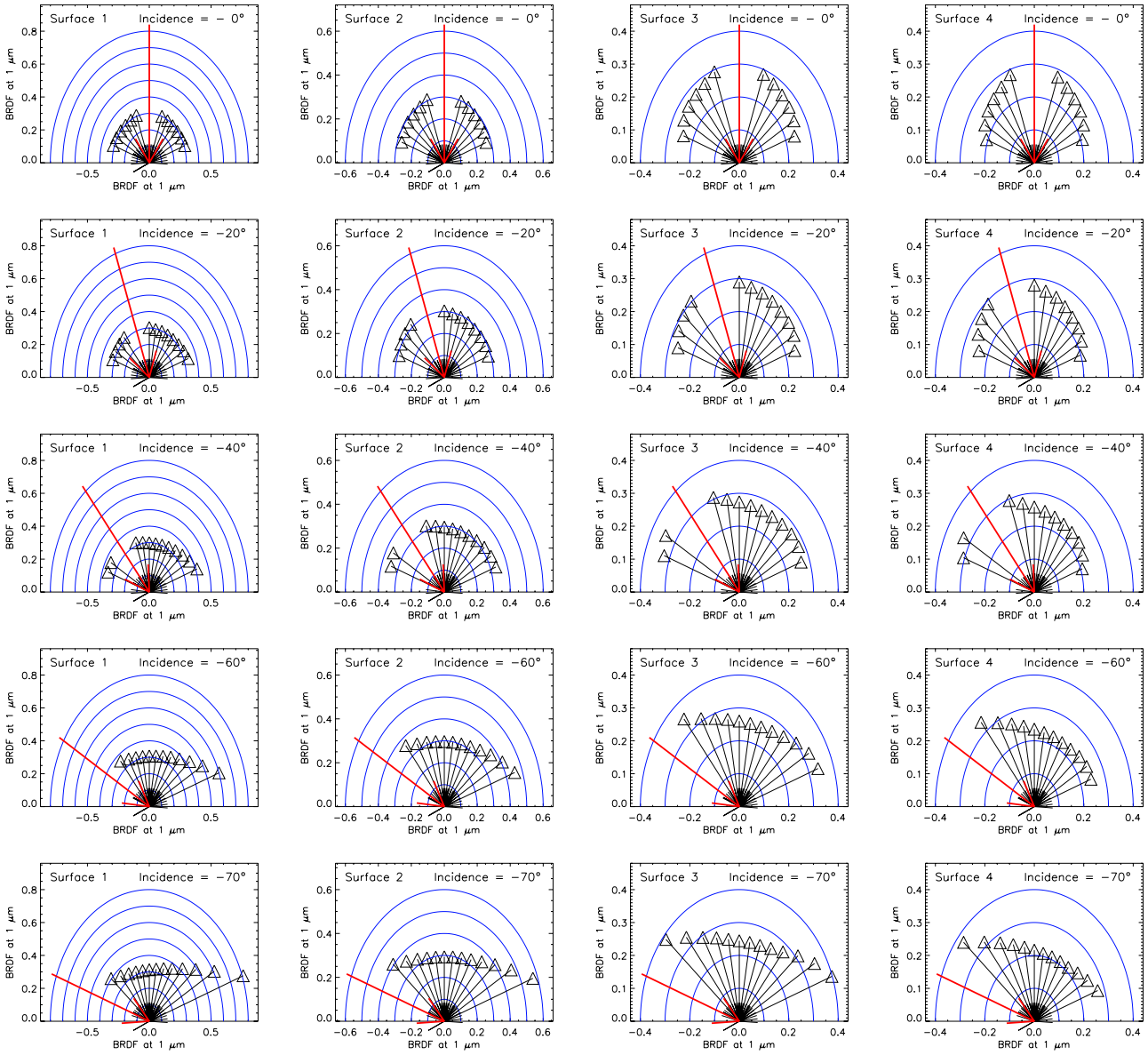

Figure 14. BRDF polar plots at 1 μm for the four different surfaces prepared with the volcanic tuff (50–100 μm) and (800–1120 μm) particle size fractions. See Figure 1 for pictures and description of these surfaces. Each column corresponds to a different surface (progressive addition of large grains on smooth surface from left to right). Each line corresponds to a different incidence angle (0°, 20°, 40°, 60°, 70°) indicated by the arrow. The effect of adding large grains on the smooth surface is a transition from a forward scattering behavior to a backscattering behavior due to the appearance of shadows at high phase angle.

sion between measurements at the same phase angle but different emission angles.

3.3. Effect of Particle Size

[50] Using radiative transfer modeling, we can compare the variations of band strength between different measurement geometries for different particle size and different particle anisotropy parameters of the SWy-1 smectite. Relationships between these parameters are shown on Figure 18 for both the 1.9 and 3-μm absorption bands. On Figure 18, we plot the relative decrease of band strength between two extreme geometries: phase angle = 0° (incidence angle = emergence angle = 0°) and phase angle = 140° (incidence angle = 70° and emergence angle = −70°). This relative variation of band strength decreases as particle size increases. For the 3-μm band, we observe large variations of the relative decrease for the lowest particle size whereas variations become smaller for the largest particles. This behavior is also apparent, but less marked, for the 1.9-μm band. These results have to be compared to a detailed study of the relationships between band strength and particle size that is presented in a companion article [*Pommerol and Schmitt*, 2008] that shows similar behaviors. We also measured a limited number of situations in the

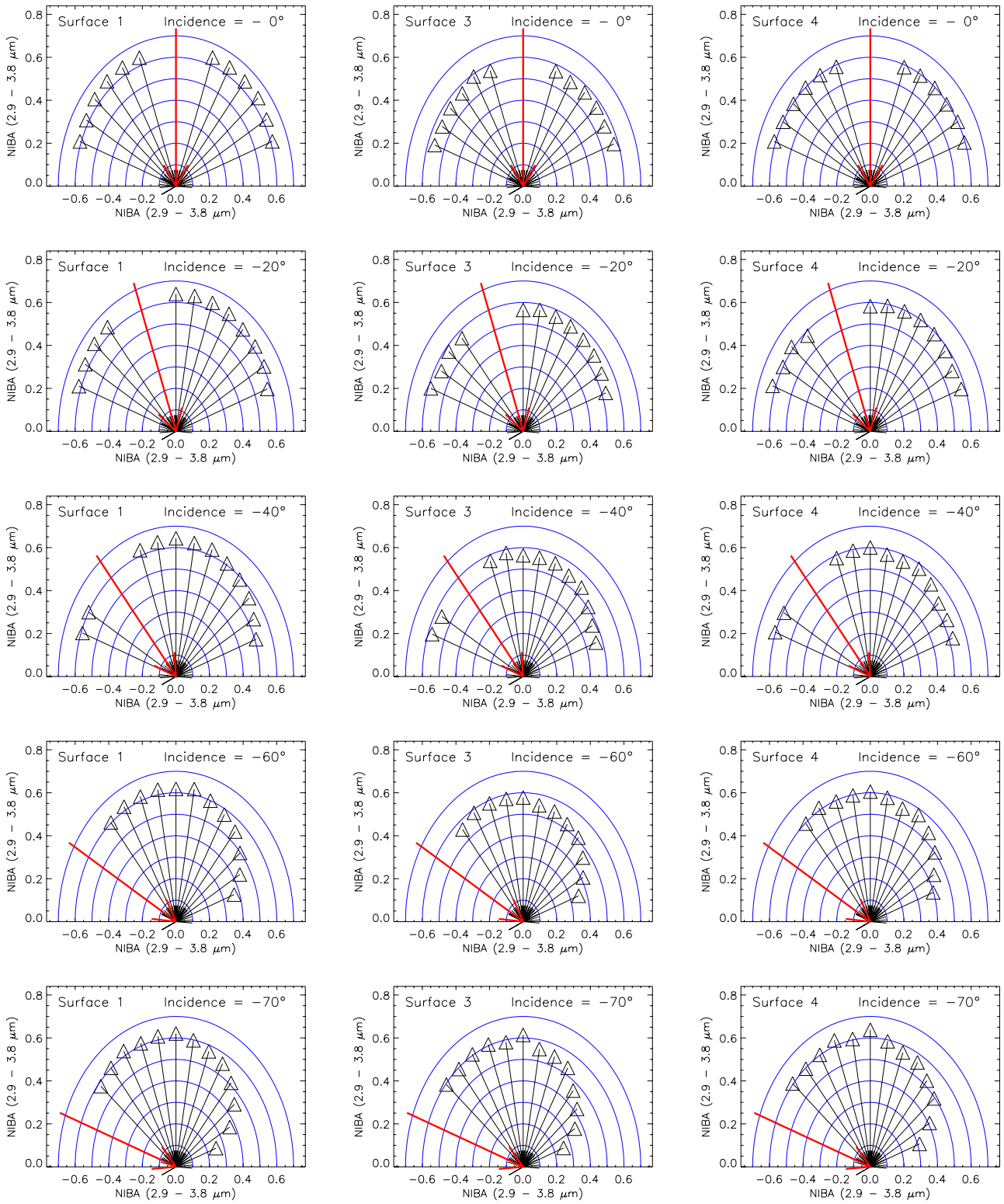

Figure 15. Polar plots of NIBA at 3 μm for three different surfaces prepared with the volcanic tuff. (left column) Smooth surface prepared with (50–100 μm) fraction. (center column) Smooth surface + 0.32 g of large grains (fraction [800–1120 μm]). (right column) Smooth surface + 0.52 g of large grains. Each row corresponds to a different incidence angle (0°, 20°, 40°, 60°, 70°) indicated by the arrow.

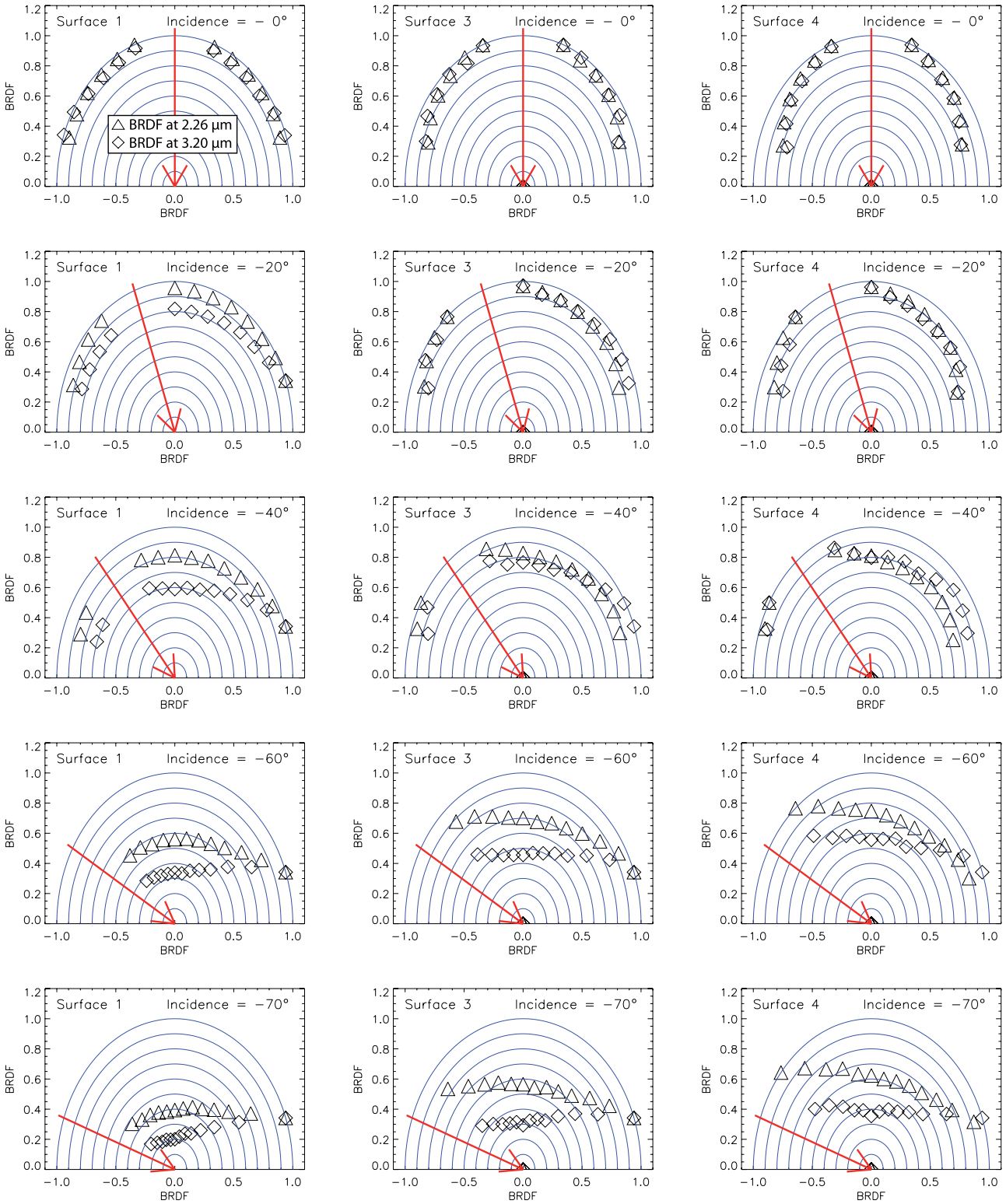

Figure 16. Comparison of BRDF behaviors in the continuum (2.26 μm) and in the 3.2 μm absorption band for the three different surfaces prepared with the volcanic tuff. Each BRDF is normalized to 1 at its maximum value for a better comparison of the BRDF shapes and evolutions. (left column) Smooth surface prepared with (50–100 μm) fraction. (center column) Smooth surface + 0.32 g of large grains (fraction [800–1120 μm]). (right column) Smooth surface + 0.52 g of large grains. Each row corresponds to a different incidence angle (0°, 20°, 40°, 60°, 70°) indicated by the arrow.

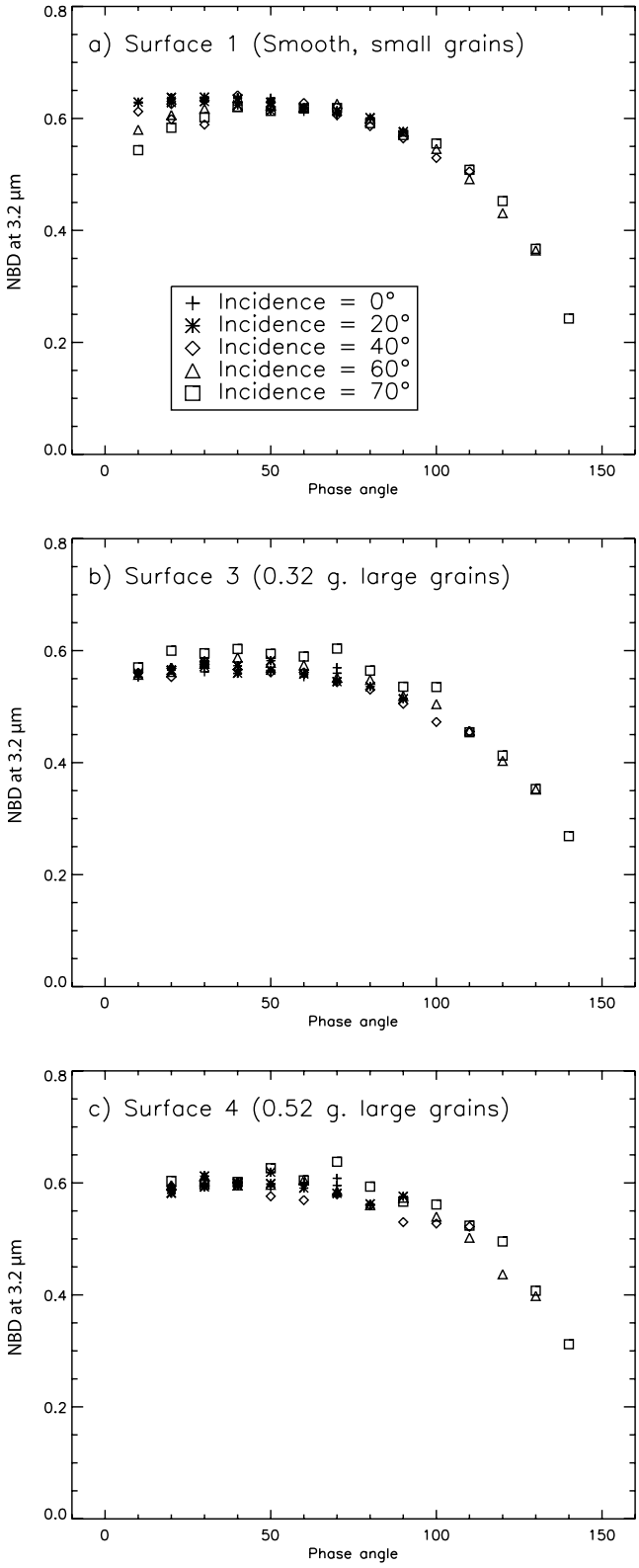

Figure 17. Evolution of NBD at 3.2 μm as a function of phase angle for three different surfaces prepared with volcanic tuff. (a) Smooth surface prepared with the [50–100 μm] fraction. (b) Smooth surface + 0.32 g of large grains (fraction [800–1120 μm]). (c) Smooth surface + 0.52 g of large grains.

laboratory to highlight the effects of particle size. Reflectance spectra of 3 different particle size fractions of the SWy-2 smectite were measured at a fixed emission angle (−30°) but with incidence angle varying between 0 and 70°, leading to phase angles between 30° and 100°. The particle size fractions used were: <25 μm, [50–100] μm, and [200–280] μm. As on modeled spectra, we calculate the decrease of the 1.9-μm BD and the 3-μm NIBA between the lowest (30°) and highest (100°) phase angles. Results are summarized in Table 1.

[51] These experimental results agree with the main conclusion obtained from modeling: phase angle effects are reduced when particle size increases. Furthermore, as expected from radiative transfer modeling (Figure 18), variations due to particle size are smaller between the middle and largest size fractions than between the smallest and middle size fractions by about one order of magnitude.

[52] We attribute the reduction of band strength at high phase angle to the strong forward scattering behavior in the absorption band due to strong reflections on particle external surface at high incidence angles. As particle size increases, the surface/volume ratio decreases and thus the amount of light scattered in the forward direction. As anisotropy of BRDF in the absorption band decreases, effect of phase angle on band strength is also attenuated.

4. Discussion

[53] Our experimental results highlight the strong influence of measurement geometry on the visible and near-infrared spectra of smectite and volcanic tuff. Both continuum and absorption bands are affected by changes in incidence and emergence angles. In the continuum, spectra of the two materials develop a positive spectral slope when phase angle increases. Measurement geometry affects the continuum and absorption regions differently, producing strong variations in band strength, especially at high phase angles. The most noticeable effect on reflectance spectra is a desaturation of the strong 3-μm absorption band that results in a reduction of absorption intensity for the highest phase angle values. The evolution of band strength appears similar for the shallower 1.9-μm band in the case of the STx-1 smectite. The main difference between the behaviors of the two H_2O absorption bands is the larger variation observed at constant low phase angles for the 1.9-μm band when incidence or emergence angles vary. For the 3-μm band, conversion of reflectance to apparent absorbance accentuates the effect of measurement geometry variations: at high phase angle, the decrease of band strength is more pronounced while dispersion increases at low phase angle. In a similar way, conversion to single scattering albedo assuming a Lambertian behavior of the surface gives raise to important variations of band strength when incidence and emergence angles vary.

[54] The scattering behavior in the continuum (forward or backward) only has a small influence on the relationship between the 3-μm band strength and phase angle as it is observed for different surfaces prepared using two different particle size fractions of volcanic tuff. Even when the continuum reflectance behavior changes from strongly forward to strongly backscattering, we observe only a small reduction of the band strength contrast between the lowest

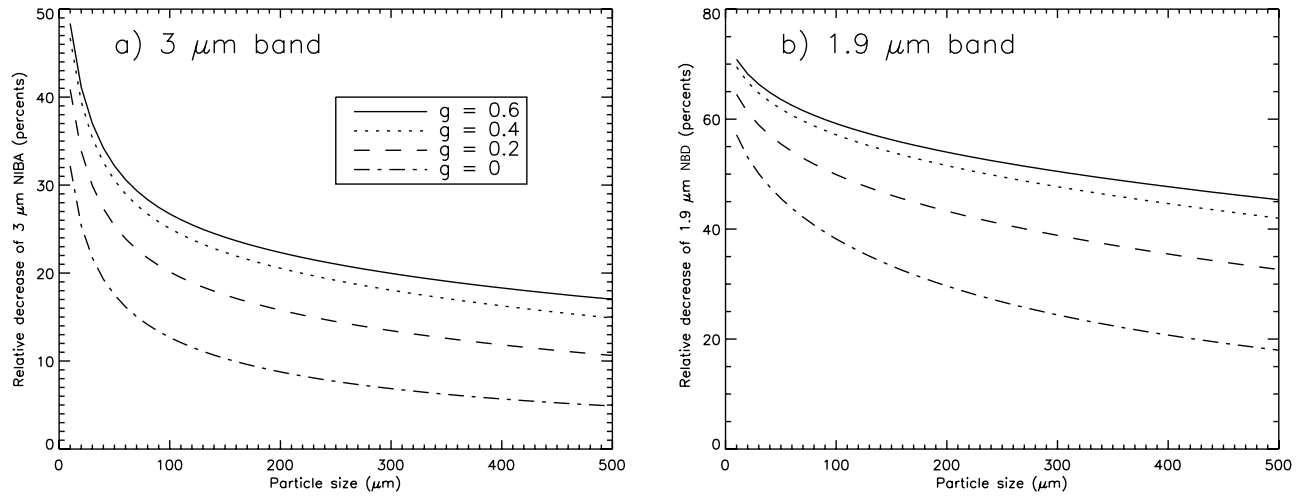

Figure 18. Relative decrease of the 3-μm band NIBA and 1.9-μm NBD (in %) between phase angle = 0° and phase angle = 140° as a function of particle size. Results from radiative transfer modeling (using optical constants of the SWy-1 smectite) with different values of scattering anisotropy: *g*.

and highest phase angles (Figure 17). This result is interesting in terms of planetary surfaces remote sensing. We can expect that the strength of the strong 3-μm band will always have a relatively similar dependence with phase angle regardless of surface texture variations that, on the other hand, can induce very strong changes of scattering behavior in the spectral continuum. This result is currently only validated for strong absorptions and may not be valid for shallower bands. We have also shown that particle size has a strong influence on the relationship between band strength and phase angle.

[55] This result can be directly applied to the case of the Martian surface. H_2O absorption bands are mapped or have been mapped by different instruments (IRS/Mariner 6&7, ISM/Phobos-2, OMEGA/Mars Express and CRISM/MRO). One of the main results of the mapping by OMEGA is a positive gradient of the 3-μm band strength from equatorial to polar regions interpreted as an enrichment of the regolith in adsorbed water [*Jouglet et al.*, 2007; *Milliken et al.*, 2007]. Most of OMEGA observations are obtained at zero emission angle (NADIR observations) but during an observation sequence incidence angle, and thus phase angle, increases from equatorial to polar regions. Thus this variation of phase angle could lead to variations of band strength non-related to water content. Our results indicate that variations of band strength due to measurement geometry variations should be limited in the case of NADIR observations because large variations of band strength occur only for phase angles above 100°. However, we cannot exclude that phase angle variations produce a small artifact of a few percents on the value of band strength calculated from observed reflectance spectra. This would lead to an underestimation of the adsorbed water gradient because the phase angle effect is the opposite from the observed mineral hydration gradient. Study of seasonal variations of regolith water content in Martian polar regions is also affected by the influence of phase angle on band strength because measurements of the same area at different seasons imply different incidences and thus phase angles. Therefore any observed difference in band strength between two different times of the Martian year should be check to ensure that it cannot be explained by the corresponding change in phase angle, using the relationship we established. If effects of measurement geometry variations are critical, spectral criteria calculated on reflectance spectra should be preferred over spectral criteria implying a conversion to apparent absorbance or single scattering albedo assuming a Lambertian surface because these conversions emphasize band strength variations, even at low phase angle. *Erard and Calvin* [1997] published a comparison of 3-μm band strength values measured on the same areas of the Martian surface successively by the IRS and ISM instruments with an interval of 20 years. Band depth at 3 μm measured by the IRS instruments are always larger (15% in average) than those measured by ISM. The authors attribute this change to the difference of measurement geometry (phase angle >55° for IRS and <5° for ISM). Our results do not support this interpretation as we always obtain, from measurements and modeling, a decrease of band depth when phase angle increases. Therefore other effects like variations of water content or amount of aerosols have to be considered.

[56] Similarly to the case of a surface mapping, any comparison of mineral hydration state that relies on a comparison of band strength between two different objects (asteroids, moons...) is also potentially affected by differences in measurement geometries between the observations.

[57] Radiative transfer modeling is able to correctly reproduce the evolutions of hydration band strength on measurement geometries obtained from experiments. How-

Table 1. Relative Decrease (in %) of Band Strength Between Phase Angle = 30° and Phase Angle = 100°[a]

	<25 μm	50–100 μm	200–280 μm
1.9 μm NBD	19.5 %	14.5 %	13.8 %
3 μm NIBA	14.7 %	9.7 %	9.2 %

[a]Experimental results with SWy-2 smectite sample.

ever, the use of a Henyey-Greenstein parameter g independent of wavelength in the model introduces many discrepancies with experimental results. Better results can be obtained if g is chosen larger in the absorption band than in the continuum around the band.

[58] This confirms the need for measurements of materials and surfaces BRDFs over large wavelength ranges, both in the laboratory and for planetary surfaces. In the case of the Martian surface, the CRISM instrument [*Murchie et al.*, 2007] already acquires such measurements of surface BRDF over a large wavelength range and hundreds of spectral channels. This data set will help in studying the relationship between both the 1.9 and 3-μm band strengths and measurement geometry on different areas and for different types of surface materials. However, because it is challenging to separate scattering effects of atmospheric aerosols from a surface anisotropic scattering behavior, laboratory measurements on analog materials and surfaces will always be necessary to help in the interpretation of such multiangular data sets.

[59] **Acknowledgments.** This work has been supported by the French "Programme National de Planétologie" from CNRS and by the "Centre National d'Etudes Spatiales". We acknowledge Olivier Brissaud for his assistance in the use of the spectro-gonio-radiometer and Sylvain Douté for his assistance in the use of the radiative transfer model. We thank P. Pinet and an anonymous reviewer for their insightful and constructive reviews.

References

Bibring, J.-P., Y. Langevin, J. F. Mustard, F. Poulet, R. Arvidson, A. Gendrin, B. Gondet, N. Mangold, P. Pinet, and F. Forget (2006), Global mineralogical and aqueous Mars history derived from OMEGA/Mars express data, *Science*, *312*, 400–404.

Bonnefoy, N. (2001), Développement d'un spectro-goniomètre pour l'étude de la réflectance bidirectionnelle des surfaces géophysiques. Application au soufre et perspectives pour le satellite Io, Ph.D. thesis, Lab. de Planét. de Grenoble—Univ. Joseph Fourier, Grenoble, France.

Brissaud, O., B. Schmitt, N. Bonnefoy, S. Douté, P. Rabou, W. Grundy, and M. Fily (2004), Spectrogonio radiometer for the study of the bidirectional reflectance and polarization functions of planetary surfaces. 1: Design and tests, *Appl. Optics*, *43*, 1926–1937.

Calvin, W. M., and R. N. Clark (1993), Spectral distinctions between the leading and trailing hemispheres of Callisto—New observations, *Icarus*, *104*, 69–78.

Chandrasekhar, S. (1960), *Radiative Transfer*, 2nd ed., 393 pp., Dover, Mineola, New York.

Clark, R. N., and T. L. Roush (1984), Reflectance spectroscopy: Quantitative analysis techniques for remote sensing applications, *J. Geophys. Res.*, *89*, 6329–6340.

Cloutis, E. A., M. A. Craig, and D. T. Bailey (2007), Bidirectional reflectance properties of orthopyroxene, *Lunar Planet. Inst. Conf. Abstr.*, 38, 1300.

Cord, A. M., P. C. Pinet, Y. Daydou, and S. D. Chevrel (2003), Planetary regolith surface analogs: optimized determination of Hapke parameters using multi-angular spectro-imaging laboratory data, *Icarus*, *165*, 414–427.

Cord, A., P. C. Pinet, Y. Daydou, and S. D. Chevrel (2005), Experimental determination of the surface photometric contribution in the spectral reflectance deconvolution processes for a simulated Martian crater-like regolithic target, *Icarus*, *175*, 78–91.

Costanzo, P. M., and S. Guggenheim (2001), Baseline studies of the clay minerals society source clays: Preface, *Clays Clay Miner.*, *49*, 371.

Douté, S., and B. Schmitt (1998), A multilayer bidirectional reflectance model for the analysis of planetary surface hyperspectral images at visible and near-infrared wavelengths, *J. Geophys. Res.*, *103*, 31,367–31,390.

Douté, S., W. M. Grundy, F. Devedeux, B. Schmitt, and O. Brissaud (2003), Experimental study of visible and IR light reflection by planetary-like granular materials, *EGS-AGU-EUG Joint Assembly*, Abstract 12152, 2003, 12152.

Erard, S., and W. M. Calvin (1997), New composite spectra of Mars, 0.4–5.7 mm, *Icarus*, *130*, 449–460.

Fischer, E. M., and C. M. Pieters (1993), The continuum slope of Mars: Bidirectional reflectance investigations and applications to Olympus Mons, *Icarus*, *102*, 185–202.

Georgiev, G. T., and J. J. Butler (2005), Bidirectional reflectance distribution function and directional-hemispherical reflectance of a Martian regolith simulant, *Opt. Eng.*, *44*, 6202–6213.

Gradie, J., and J. Veverka (1986), The wavelength dependence of phase coefficients, *Icarus*, *66*, 455–467.

Grundy, W. M., S. Douté, and B. Schmitt (2000), A Monte Carlo ray-tracing model for scattering and polarization by large particles with complex shapes, *J. Geophys. Res.*, *105*, 29,290–29,314.

Guggenheim, S., and A. F. Koster Van Groos (2001), Baseline studies of the clay minerals society source clays: Thermal analysis, *Clays Clay Miner.*, *49*, 433–443.

Gunderson, K., B. Lüthi, P. Russell, and N. Thomas (2007), Visible/NIR photometric signatures of liquid water in Martian regolith stimulant, *Planet. Space Sci.*, *55*, 1272–1282.

Hapke, B. (1993), *Theory of Reflectance and Emittance Spectroscopy. Topics in Remote Sensing*, Cambridge Univ. Press, Cambridge, U.K.

Hapke, B. (2002), Bidirectional reflectance spectroscopy. 5: The coherent backscatter opposition effect and anisotropic scattering, *Icarus*, *157*, 523–534.

Henyey, L. G., and J. L. Greenstein (1941), Diffuse radiation in the galaxy, *Apj.*, *93*, 70–83.

Johnson, J. R., M. K. Shepard, W. M. Grundy, R. V. Morris, and T. S. White (2007), Spectrogoniometric measurements and models of Mars analog soils, *Lunar Planet. Inst. Conf. Abstr.*, *38*, 1288.

Jouglet, D., F. Poulet, R. E. Milliken, J. F. Mustard, J.-P. Bibring, Y. Langevin, B. Gondet, and C. Gomez (2007), Hydration state of the Martian surface as seen by Mars Express OMEGA. 1: Analysis of the 3 μm hydration feature, *J. Geophys. Res.*, *112*, E08S06, doi:10.1029/2006JE002846.

Kamei, A., and A. M. Nakamura (2002), Laboratory study of the bidirectional reflectance of powdered surfaces: On the asymmetry parameter of asteroid photometric data, *Icarus*, *156*, 551–561.

McCord, T. B., et al. (1999), Hydrated salt minerals on Europa's surface from the Galileo near-infrared mapping spectrometer (NIMS) investigation, *J. Geophys. Res.*, *104*, 11,827–11,851.

Milliken, R. E., and J. F. Mustard (2005), Quantifying absolute water content of minerals using near-infrared reflectance spectroscopy, *J. Geophys. Res.*, *110*, E12001, doi:10.1029/2005JE002534.

Milliken, R. E., and J. F. Mustard (2007a), Estimating the water content of hydrated minerals using reflectance spectroscopy. I: Effects of darkening agents and low-albedo materials, *Icarus*, *189*, 550–573.

Milliken, R. E., and J. F. Mustard (2007b), Estimating the water content of hydrated minerals using reflectance spectroscopy. II: Effects of particle size, *Icarus*, *189*, 574–588.

Milliken, R. E., J. F. Mustard, F. Poulet, D. Jouglet, J.-P. Bibring, B. Gondet, and Y. Langevin (2007), Hydration state of the Martian surface as seen by Mars Express OMEGA. 2: H_2O content of the surface, *J. Geophys. Res.*, *112*, E08S07, doi:10.1029/2006JE002853.

Morris, R. V., W. W. Mendell, and S. C. Neely (1982), Application of Kubelka-Munk theory of diffuse reflectance to geologic problems: The role of scattering, *Geophys. Res. Lett.*, *9*, 113–116.

Murchie, S., et al. (2007), Compact Reconnaissance Imaging Spectrometer for Mars (CRISM) on Mars Reconnaissance Orbiter (MRO), *J. Geophys. Res.*, *112*, E05S03, doi:10.1029/2006JE002682.

Mustard, J. F., and C. M. Pieters (1989), Photometric phase functions of common geologic minerals and applications to quantitative analysis of mineral mixture reflectance spectra, *J. Geophys. Res.*, *94*, 13,619–13,634.

Pieters, C. M. (1983), Strength of mineral absorption features in the transmitted component of near-infrared reflected light—First results from RELAB, *J. Geophys. Res.*, *88*, 9534–9544.

Pommerol, A., and B. Schmitt (2008), Strength of the H_2O near-infrared absorption bands in hydrated minerals: Effects of particle size and correlation with albedo, *J. Geophys. Res.*, *113*, E10009, doi:10.1029/2007JE003069.

Rivkin, A. S., J. K. Davies, J. R. Johnson, S. L. Ellison, D. E. Trilling, R. H. Brown, and L. A. Lebofsky (2003), Hydrogen concentrations on C-class asteroids derived from remote sensing, *Meteor. Planet. Sci.*, *38*, 1383–1398.

Roush, T. L. (2005), Near-infrared (0.67–4.7 μm) optical constants estimated for Montmorillonite, *Icarus*, *179*, 259–264.

Ryskin, Y. (1974), The vibrations of protons in minerals: Hydroxyl, water and ammonium, in *The Infrared Spectra of Minerals*, edited by V. C. Farmer, pp. 137–182, Mineral. Soc., London.

Shepard, M. K., and P. Helfenstein (2007), A test of the Hapke photometric model, *J. Geophys. Res.*, *112*, E03001, doi:10.1029/2005JE002625.

Shkuratov, Y. G., and Y. S. Grynko (2005), Light scattering by media composed of semitransparent particles of different shapes in ray optics approximation: consequences for spectroscopy, photometry, and polarimetry of planetary regoliths, *Icarus*, *173*, 16–28.

Shkuratov, Y. G., D. G. Stankevich, D. V. Petrov, P. C. Pinet, A. M. Cord, Y. H. Daydou, and S. D. Chevrel (2005), Interpreting photometry of regolith-like surfaces with different topographies: shadowing and multiple scattering, *Icarus*, *173*, 3–15.

A. Pommerol and B. Schmitt, Laboratoire de Planétologie de Grenoble, Université J. Fourier, CNRS/INSU, Bât. D de Physique, B.P. 53, 38041 Grenoble Cedex 9, France. (antoine.pommerol@obs.ujf-grenoble.fr)